

Spin qubit shuttling between coupled quantum dots with inhomogeneous Landé g-tensors

Zhi-Hai Liu,^{1,*} Xiao-Fei Liu,^{1,†} and H. Q. Xu^{1,2,‡}

¹*Beijing Academy of Quantum Information Sciences, Beijing 100193, China*

²*Beijing Key Laboratory of Quantum Devices, Peking University, Beijing 100871, China*

(Dated: February 17, 2026)

By utilizing the site-dependent spin quantization axis in semiconductor quantum dot (QD) arrays, shuttling-based spin qubit gates have become an appealing approach to realize scalable quantum computing due to the circumvention of using high-frequency driving fields. The emergence of a spin deviation from the local quantization axis of one residing QD is the prerequisite to implement the qubit gates. In this work, we study the non-adiabatic dynamics of a spin qubit shuttling between coupled QDs with inhomogeneous Landé g-tensors and a small magnetic field. The spin dynamics is analyzed through solving the time-dependent Schrödinger equation of the qubit under the effects of spin-orbit interaction and rapid ramping inter-dot detuning. The precondition, imposed on the ramping time and the tunnel-coupling strength, to ensure a high-fidelity inter-dot transfer is estimated. We then calculate the change in the spin orientation of a transferred qubit, and study the dependences of the spin deviation on the difference in the quantization axes of the two QDs, the tunnel-coupling strength, and the ramping time. We also demonstrate that the effect of multiple rounds of inter-dot bidirectional shuttling can be captured by an operator matrix, and evaluate the idling times required for realizing the single-qubit Pauli-X and Pauli-Y gates. Intriguingly, it is confirmed that a generalized Hadamard gate can be achieved through tuning the idling times.

I. INTRODUCTION

Semiconductor quantum dots (QDs) have attracted extensive attentions owing to their great potential for implementing universal quantum computation^{1–4}. Experimentally, the single- and two-qubit gate fidelities of spin qubits in silicon-based^{5–9} and Ge-based^{10–12} QDs have exceeded the quantum error correction threshold, thereby paving the way for the practical implementation of noisy intermediate-scale quantum devices¹³. Most recently, the engineering of spin qubit shuttling in dense QD arrays has reduced the need for high-frequency oscillating drivers in qubit manipulation^{14–23}. To elaborate, conveyor-mode shuttling facilitates high-fidelity state transfer over extended distances^{14–18}, whereas coherent spin shuttling between QDs enables the realization of qubit quantum logic gates^{19–23}. Importantly, these techniques also alleviate crosstalk and heating effects in large-scale scalable quantum computing^{24–29}.

Essentially, the shuttling-based single-qubit logic gates in Refs. 21–23 are established on the Larmor precession of a hole (or electron) spin qubit transferred into one target QD. The emergence of a deviation from the local spin quantization axis is the basic premise for implementing the qubit gates³⁰. This evidently requires a non-adiabatic transfer process, otherwise the spin direction of a shuttled qubit is bound to be aligned with the local axis^{31–33}. Remarkably, it goes against to the suppression of Landau-Zener transitions (LZTs), which leads to the reduction of the fidelity of an inter-dot transfer^{34–38}. Equipped with precise control of the inter-dot detuning, the logic gates are actually implemented in an operational regime that not only enables high-fidelity qubit transfer but also ensures a well-defined spin deviation. In contrast to studies on LZT processes^{36–39}, however, the spin deviation of

qubits transferred to the target QD has thus far received insufficient theoretical attention. Accordingly, there is an urgent need to thoroughly analyze the evolution of qubit spin orientation following non-adiabatic inter-dot shuttling processes.

Considering a non-orthogonal deviation of the transferred qubit from the local spin-quantization axis, Pauli-X or Pauli-Y qubit gates are generally implemented via multiple rounds of inter-dot transfer^{21–23}. Interestingly, Ref. 40 reported an alternative theoretical approach for realizing qubit gates along unidirectional simultaneous transport in double QDs. Therein, quaternionic algebra has thus far been harnessed for the inverse design of single-qubit phase and NOT gates, in accordance with the system's Hamiltonian structure^{40,41}. By comparison, state-of-the-art experimental logic protocols leveraging multiple-round transfer driven by inter-dot detuning exhibit substantial flexibility^{21–23}, albeit at the expense of prolonged gate operation times. Particularly, fine-tuning the idling times within the QDs constitutes an indispensable prerequisite for implementing shuttling-based single-qubit gates^{21–23}. Hitherto, to the best of our knowledge, the dependence of the requisite times on the characteristics of inter-dot shuttling still remains to be elucidated for pursuing high-fidelity and more sophisticated shuttling-based qubit gates.

In this work, we focus on the non-adiabatic dynamics of a spin qubit shuttling between two coupled QDs with inhomogeneous Landé g-tensors^{42–45}, as such the spin quantization axis is site-dependent in a small magnetic field. Firstly, we evaluate the infidelity of an inter-dot transfer of the qubit under the effects of spin-orbit interaction (SOI)^{20,28} and the rapid ramping inter-dot detuning^{30,34}. The precondition, imposed on the ramping time and the tunnel-coupling strength, is estimated

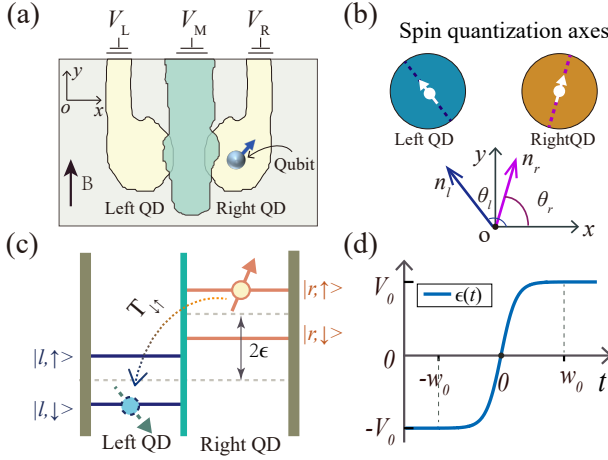


FIG. 1. (a) Schematic of coupled quantum dots, i.e., left QD and right QD, occupied by a single spin qubit, in which $V_{L/R}$ and V_M represent the left/right plunger-gate and middle barrier-gate potentials. (b) The spin quantization axes of the two QDs in a low magnetic field B applied in the y -direction, i.e., $\mathbf{n}_{l/r} = (\cos \theta_{l/r}, \sin \theta_{l/r}, 0)$ with $\theta_{l/r}$ being the direction angle of the left/right dot. (c) The “spin-flipped” tunneling $T_{\downarrow\uparrow}$ of a qubit between the two QDs, with $|l/r, \uparrow\rangle$ and $|l/r, \downarrow\rangle$ indicating the local Zeeman-splitting states and ϵ sizing the inter-dot detuning. (d) A specific ramping up of $\epsilon(t) = V_0 \tanh(\pi t/w_0)$ to implement a leftward inter-dot transfer, with w_0 being the ramping time.

to reduce the infidelity of the inter-dot transfer. Following the realization of a high-fidelity ($> 99\%$) transfer, we subsequently study the change in the spin orientation of a transferred qubit, thereby revealing the flexibility of deviation from the spin-quantization axis of the target QD. Besides, we show that such deviation can be reflected by the reversal of the spin orientation of a qubit undergoing one round of inter-dot transfer. By introducing an operation matrix describing the overall effect of multiple rounds of inter-dot shuttling protocols, the requisite idling times are further evaluated in the implementation of shuttling-based single-qubit gates. In addition to the realization of Pauli-X and Pauli-Y gates, we demonstrate that a generalized Hadamard gate can also be attained with tuning the idling times.

II. THE EFFECTIVE HAMILTONIAN OF A SPIN QUBIT IN DOUBLE QDS

The coupled QDs we consider is occupied by a single hole (or electron) spin qubit and with a small magnetic field B applied in the y direction, just as shown in Fig. 1(a). Considering the inhomogeneity in the Landé g-tensors of the QDs, the qubit spin-quantization axis is thereby site-dependent under the transverse magnetic field. For simplicity, the quantization axes can be assumed to be laid in the x - y plane, with $\hat{n}_{l/r} =$

$(\cos \theta_{l/r}, \sin \theta_{l/r}, 0)$ characterizing the axis direction of the left/right QD and with $\theta_l \neq \theta_r$ [see Fig. 1(b)]. Similar to self-assembled QDs, inhomogeneity in the transverse components of hole Landé g-tensors can be attributed to fluctuations in shape symmetry, strain gradients, and structural deformations of the low-dimensional nanostructures^{46–48}. For the gate-defined QDs focused on in this work, the transverse inhomogeneous features can also be regulated by the respective gate potentials⁴⁴ [e.g., $V_{L,R}$ and V_M in Fig. 1(a)].

Notably, when hyperfine interactions with nuclear spins are considered, random hyperfine interactions can also induce differences in the spin-quantization axes of two coupled QDs^{49–54}, in either the absence or presence of a weak external magnetic field. Meanwhile, nuclear fluctuations will disrupt the deterministic distinction between the spin axes (a prerequisite for shuttling-based qubit gates) and exert deleterious effects on the qubit spin coherence^{52–54}. To mitigate such adverse impacts, a lower limit is thus imposed on the magnetic-field strength, specifically requiring B to exceed the magnitude of the averaged hyperfine fields^{55–57}. Besides, the constraints on the field strength for defining well-behaved spin qubits in QDs are detailed in Appendix A.

Based on the orientation of the local spin-quantization axis $\hat{n}_{\kappa=l,r}$, the low-energy Zeeman splitting states of the QDs satisfy the relation $(\boldsymbol{\sigma} \cdot \hat{n}_{\kappa})|\kappa, \uparrow / \downarrow\rangle = \pm |\kappa, \uparrow / \downarrow\rangle$, where $|\kappa, \uparrow / \downarrow\rangle$ denotes the respective upper/lower Zeeman-splitting levels and $\boldsymbol{\sigma} = \{\sigma_x, \sigma_y, \sigma_z\}^T$ represents the spin Pauli matrices. The corresponding energy splitting is denoted by $\Delta_{z,\kappa}$. Besides, a mismatch between the Zeeman splitting of two coupled QDs can give rise to a spin bottleneck during resonant tunneling⁵⁸. Accordingly, we assume that the energy splitting is site-independent, i.e., $\Delta_{z,\kappa} \equiv \Delta_z$, to pinpoint the impact of disparities in the spin-quantization axes of the QDs.

Analogous to the effect of Rashba SOI^{59–63}, a difference in the QDs’ spin-quantization axes, i.e., $\theta_l \neq \theta_r$ will lead to the breaking of spin-conservation rules during the inter-dot tunneling. Then, the effective Hamiltonian describing the single spin qubit in the coupled QDs can be written as

$$H_0 = \sum_{\sigma=\uparrow,\downarrow} (T_{\sigma\sigma}|l, \sigma\rangle\langle r, \sigma| + T_{\bar{\sigma}\bar{\sigma}}|l, \bar{\sigma}\rangle\langle r, \bar{\sigma}| + \text{h.c.}) + \sum_{\kappa, \sigma} E_{\kappa, \sigma}|\kappa, \sigma\rangle\langle \kappa, \sigma| \quad (1)$$

Here, $E_{l,\uparrow/\downarrow} = -\epsilon \pm \Delta_z/2$ and $E_{r,\uparrow/\downarrow} = \epsilon \pm \Delta_z/2$ indicate the spin-dependent on-site energies, with ϵ specifying the inter-dot detuning and determined by the plunger-gate potentials $V_{L,R}$ in Fig. 1(a). $T_{\sigma\sigma}$ and $T_{\bar{\sigma}\bar{\sigma}}$ quantify the amplitudes for a qubit tunneling from the right-QD state $|r, \sigma\rangle$ to the respective spin states $|l, \sigma\rangle$ and $|l, \bar{\sigma}\rangle$ of the other QD. Nominally, they can be referred to as the “spin-conserved” and “spin-flipped” tunneling amplitudes. Then, by incorporating the effect of SOI in the

inter-dot tunneling processes^{62,63}, the amplitudes can be analytically derived as

$$\begin{aligned} T_{\uparrow\uparrow/\downarrow\downarrow} &= T_0 (\cos \varphi_{\text{so}} \cos \theta_\delta \pm i \sin \varphi_{\text{so}} \sin \theta_0) , \\ T_{\uparrow\downarrow/\downarrow\uparrow} &= T_0 (i \cos \varphi_{\text{so}} \sin \theta_\delta \pm \sin \varphi_{\text{so}} \cos \theta_0) , \end{aligned} \quad (2)$$

in which T_0 indicates the tunnel-coupling strength dominated by the barrier-gate potential V_M in Fig. 1(a), $\theta_{0/\delta} = (\theta_r \pm \theta_l)/2$, and φ_{so} captures the concomitant effect of SOI during the inter-dot tunneling. In fact, it depicts the spin rotation phase, named as the Aharonov-Casher (AC) phase, acquired by a transferred qubit under the interplay between the SOI and an external magnetic field⁶⁴⁻⁶⁶. Specifically, the AC phase can be evaluated as $\varphi_{\text{so}} = 2d/\ell_{\text{so}}$, in which $2d$ characterizes the inter-dot distance and ℓ_{so} indicates the spin-orbit length⁶⁶. Please refer to Appendix A for the details. Clearly, the presence of a nonzero AC phase and with $\varphi_{\text{so}} \neq n\pi$ ($n = 1, 2, 3, \dots$) can also lead to the emergence of “spin-flipped” tunneling [see Fig. 1(c)], even without disparities in the QDs’ spin-quantization axes, i.e., $\theta_\delta = 0$.

III. NON-ADIABATIC DYNAMICS OF SPIN QUBIT SHUTTLING BETWEEN QDS

Enabled by the inter-dot tunnelings in Eqs. (2), a spin qubit can move between the QDs along a substantial change in the detuning⁶⁷⁻⁶⁹. In order to realize a leftward inter-dot transfer, the detuning ϵ is expediently modulated as $\epsilon(t) = V_0 \tanh(\pi t/w_0)$, with $V_0 \gg \max\{\Delta_z, T_0\}$ and w_0 being the ramping time [see Fig. 1(d)]. The general results we will obtain below definitely can be extended to the scenario of other rising profiles³⁸. Concretely, Fig. 2(a) show the energy spectrum of the single qubit as a function of ϵ , with $\Delta_0 = \Delta_z/2$ being the unit of energy. The four energies of $H_0(\epsilon)$ are represented by $E_{j=1-4}(\epsilon)$, and with $|\Psi_j\rangle$ indicating the energy states.

Theoretically, an adiabatic transfer corresponds to the case of $w_0 \rightarrow \infty$, and this can be reflected by the variations of $|\Psi_{1,2}\rangle$ versus ϵ . Expanded in the normalized local basis of $\{e^{i\phi_0}|l, \uparrow\rangle, e^{-i\phi_0}|l, \downarrow\rangle, e^{i\phi_\delta}|r, \uparrow\rangle, e^{-i\phi_\delta}|r, \downarrow\rangle\}$ with $\phi_{0/\delta} = [\arg(T_{\uparrow\downarrow}) \pm \arg(T_{\uparrow\uparrow})]/2$, the two lower-energy states can be presented as

$$|\Psi_1\rangle = \begin{pmatrix} \sin \alpha \cos \chi_1 \\ \cos \alpha \sin \chi_1 \\ \cos \alpha \cos \chi_1 \\ -\sin \alpha \sin \chi_1 \end{pmatrix}, |\Psi_2\rangle = \begin{pmatrix} -\cos \alpha \sin \chi_2 \\ \sin \alpha \cos \chi_2 \\ \sin \alpha \sin \chi_2 \\ \cos \alpha \cos \chi_2 \end{pmatrix}, \quad (3)$$

in which $\chi_n = [2 \arccos(T_0 \sin \beta/|E_n|) + \pi]/4$ and $\alpha = \arccos(\epsilon/\Gamma_0)/2$, with $\Gamma_0 = \sqrt{\epsilon^2 + T_0^2 \cos^2 \beta}$, and $\beta = \arccos(|T_{\sigma\sigma}|/T_0)$. Besides, the lower energies are calculated as $E_{1/2}(\epsilon) = -\sqrt{(\Delta_0 \pm \Gamma_0)^2 + T_0^2 \sin^2 \beta}$. On the basis of $\alpha, \chi_n \doteq \pi/2$ at the initial stage of $\epsilon = -V_0$, a qubit preset in the spin state $|r, \downarrow\rangle$ of the right QD is

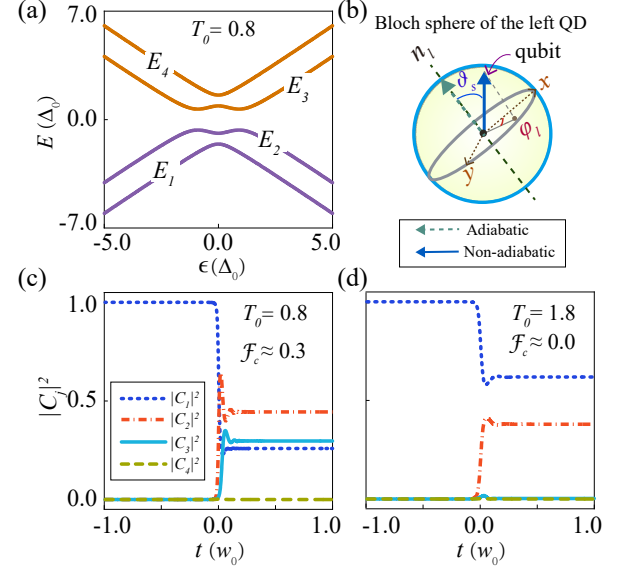


FIG. 2. (a) Energy spectrum of the single qubit as a function of ϵ with $\theta_r = 0.46\pi$, $\theta_l = 1.11\pi$, $\varphi_{\text{so}} = 0.12\pi$, $T_0 = 0.8$, and Δ_0 being the unit of energy. (b) The spin orientation of a leftward transferred qubit defined in the Bloch sphere of the left QD with \hat{n}_l specifying the pole axis and the dashed/solid arrow indicating the spin direction after undergoing a adiabatic/non-adiabatic inter-dot transfer. (c) and (d) The time evolutions of $|C_{j=1-4}(t)|^2$ for a qubit preset in the ground-state (E_1) energy level with different T_0 and $\epsilon = V_0 \tanh(\pi t/w_0)$, in which $V_0 = 10$, $w_0 = 6t_0$, and $t_0 = \pi \Delta_0/\hbar$. In addition, the infidelity of the leftward inter-dot transfer \mathcal{F}_c is indicated in each case.

actually kept in the $|\Psi_{1/2}\rangle$ energy state. As ϵ increases to V_0 , the parameter α changes to 0, and Eq. (3) implies that the qubit will transfer to the state $|l, \downarrow\rangle / |\uparrow\rangle$ of the other QD. Thus, in this case, the spin orientation of a transferred qubit is aligned with the spin quantization axis (\hat{n}_l) of the target QD, just as shown in Fig. 2(b).

However, within the non-adiabatic regime characterized by a finite w_0 , transitions between different energy levels of $H_0(\epsilon)$ will complicate the inter-dot transfer. Definitely, at a fixed time t (of a constant ϵ), the evolving state of the qubit can be expanded as $\Phi(t) = \sum_{j=1}^4 C_j(t)|\Psi_j(t)\rangle$. The time evolution of the combination coefficient $C_j(t)$ is governed by the time-dependent Schrödinger equation $i\hbar\partial_t\Phi(t) = H_0(\epsilon)\Phi(t)$, which can be expanded as

$$i \frac{dC_j(t)}{dt} + i \sum_{j'=1}^4 \mathcal{T}_{j,j'}(t)C_{j'}(t) = \frac{E_j(t)}{\hbar}C_j(t), \quad (4)$$

with \hbar being the Planck constant and $\mathcal{T}_{j,j'}(t) = \langle \Psi_j(t) | \partial_t | \Psi_{j'}(t) \rangle$ characterizing the temporal transition elements. Based on Eq. (3), it is found that the diagonal elements $\mathcal{T}_{j,j} = 0$, and the specific forms of the off-diagonal elements $\mathcal{T}_{j,j'}$ with $j \neq j'$ can refer to Appendix B. For a qubit initialized in the ground-state

energy level at $t = -w_0$, which means $C_1(-w_0) = 1$ and $C_{2-4}(-w_0) = 0$, Figs. 2(c) and 2(d) exhibit the specific time evolutions of $|C_j(t)|^2$ with two different T_0 . Because $\mathcal{T}_{j,j'}(t) \propto \text{sech}^2(\pi t/w_0)$, it is evident that $|C_{j=1-3}(t)|^2$ subject to a rapid change around $t = 0$, and the qubit will evolve into a stable state as t increases to w_0 . In addition to the transition between the two low-energy $E_{1,2}$ levels, the considerable magnitude of $|C_3(w_0)|^2$ observed in Fig. 2(c) for a smaller T_0 indicates a high probability of the qubit transition to the E_3 level.

Using the fact of $|\Psi_{3/4}(w_0)\rangle \doteq |r,\downarrow/\uparrow\rangle$, the transitions to the higher-energy $E_{3,4}$ levels actually prevent a leftward transfer, named as the LZTs. Quantitatively, the infidelity of the inter-dot transfer can be estimated as $\mathcal{F}_c = |C_3(w_0)|^2 + |C_4(w_0)|^2$. As compared with the LZTs for a charged qubit^{35,36}, the presence of spin-dependent tunnelings between the QDs complicates the transition processes. Dependent on the initial spin state of the qubit, Fig. 3(a) shows that \mathcal{F}_c exhibits a distinct feature versus β . It actually depicts the difference in the QDs' spin-quantization axes, i.e., $\beta = \theta_\delta$, for $\varphi_{\text{so}} = 0$. Specifically, \mathcal{F}_c is shown to be insensitive to the change of β when the qubit is preset in the spin-down state $|r,\downarrow\rangle$, i.e., loaded in the E_1 energy level. By contrast, \mathcal{F}_c displays a strong dependence of β if prepared in the spin-up state $|r,\uparrow\rangle$, i.e., set in the E_2 level. Clearly, \mathcal{F}_c can attain its peak around $\beta = \pi/4$ under the coordination of the “spin-flipped” and “spin-conserved” tunnelings.

By analogy to the conventional LZT theory⁷⁰⁻⁷³, the infidelity of an inter-dot transfer is dependent on the rate of change of ϵ , i.e., $\eta_0 = \partial\epsilon(t)/\partial t$ at $t = 0$. Thereby, the respective dependence relations in Fig. 3(a) can be approximately evaluated as

$$\mathcal{F}_c \simeq \begin{cases} e^{-\pi T_0^2/(\hbar\eta_0)} & \forall \Phi(-w_0) = |r,\downarrow\rangle \\ \sum_{j=1}^2 \gamma_j e^{-\pi\gamma_j T_0^2/(\hbar\eta_0)} & \forall \Phi(-w_0) = |r,\uparrow\rangle, \end{cases} \quad (5)$$

with $\gamma_{1/2} = [1 \pm \cos(2\beta)]/2$. Accordingly, the increase of T_0 can lead to the reduction of \mathcal{F}_c . Moreover, Fig. 3(b) shows the magnitude of \mathcal{F}_c as a function of w_0 and T_0 . Herein, given that $\eta_0 = \pi V_0/w_0$, the lower threshold of T_0 for realizing high-fidelity transfer will decrease with the extension of w_0 .

Upon achieving high-fidelity transfer, it is important to note that in Fig. 2(d), both $|C_1|^2$ and $|C_2|^2$ remain substantially non-zero in the final stable state ($t = w_0$). This observation directly indicates a deviation of the transferred qubit from the spin quantization axis of the target (left) QD. Addressed concretely, based on the identity $|\Psi_{1/2}(w_0)\rangle \doteq |l,\downarrow/\uparrow\rangle$, the deviation angle can be calculated as

$$\vartheta_s = 2 \arccos(|C_2(w_0)/C_1(w_0)|). \quad (6)$$

In addition, we can calibrate the azimuthal angle of the transferred qubit, defined within the Bloch sphere of the target QD [see Fig. 2(b)], using the relation $\varphi_l = 2\phi_0 + \varphi_z$ with $\varphi_z = \arg[C_2(w_0)/C_1(w_0)]$. In fact, deviation from

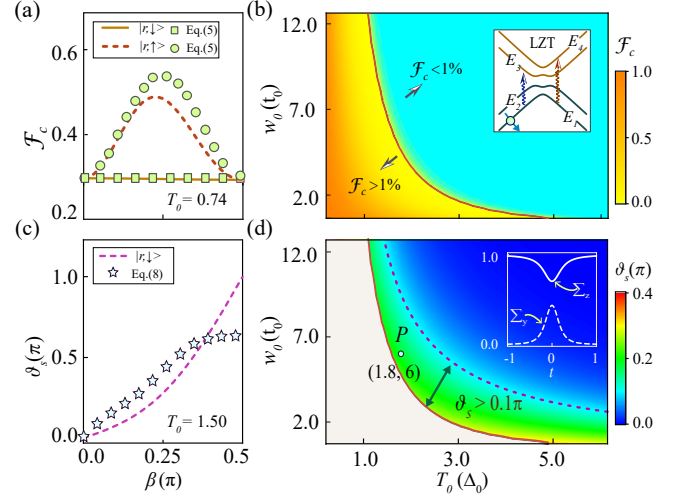


FIG. 3. (a) The infidelity of an inter-dot transfer \mathcal{F}_c as a function of β for a qubit initialized in different spin states of the right QD, with $V_0 = 10$, $T_0 = 0.74$, and $w_0 = 7.2t_0$. In addition to the numerical results (see lines), the discrete symbols specify the approximations from Eq. (5). (b) The magnitude of \mathcal{F}_c in terms of T_0 and w_0 for an initial spin-down qubit with $\beta = 0.2\pi$. The yellow- and cyan-colored regions correspond to the parameter ranges with $\mathcal{F}_c > 1\%$ and $\mathcal{F}_c < 1\%$, respectively, while the solid curve denotes the boundary between these two regions. Besides, the inset exhibits the possible LZTs. (c) For an initial spin-down qubit, the value of its spin-deviation angle ϑ_s as a function of β , with $T_0 = 1.5$ and $w_0 = 7.2t_0$. Here, the dashed curve represents the numerical results, while the discrete symbols specify the analytic results from Eq. (8). (d) The numerical distribution of ϑ_s within the range of $\mathcal{F}_c < 1\%$ in (b), with the doubled-head arrow signifying the region of $\vartheta_s > 0.1\pi$. In addition, the inset exhibits the time dependence of $\Sigma_{y,z}$ at the P point with $T_0 = 1.8$ and $w_0 = 6t_0$.

the local spin quantization axis (\hat{n}_l) stems from the interplay of spin-dependent inter-dot tunnelings. Figure 3(c) illustrates that the spin orientation of a transferred qubit tends to be parallel ($\vartheta_s = 0$) or anti-parallel ($\vartheta_s = \pi$) to the local axis in the absence of the “spin-flipped” or “spin-conserved” tunneling, i.e., when $\beta = 0$ or $\pi/2$. From an alternative prospective, it indicates two parallel or antiparallel spin quantization axes of the QDs for $\varphi_{\text{so}} = 0$. More interestingly, Fig. 3(d) illustrates that at a fixed (different) value of β , the deviation angle ϑ_s can also be regulated by the two controllable parameters T_0 and w_0 . Herein, the lower limit of ϑ_s (where $\vartheta_s = 0$) can be reached as T_0 or $w_0 \rightarrow \infty$, corresponding to the adiabatic limit. The upper limit of ϑ_s is approximately set by the disparity between the local spin axes in Fig. 1(b), i.e., $|\theta_l - \theta_r|$, as the parameters are tuned toward the threshold boundary for high-fidelity transfer.

From an analytical standpoint, the variation trend of ϑ_s can be captured by the dynamics of an effective two-level system (TLS), owing to the suppression of transitions to the $E_{3,4}$ levels. Using Eq. (4), the effective

Hamiltonian describing the TLS defined in the 2D lower-energy state subspace $\{|\Psi_1(t)\rangle, |\Psi_2(t)\rangle\}$ is given by

$$H_{\text{eff}} = \Sigma_z(t) \begin{pmatrix} 1 & 0 \\ 0 & -1 \end{pmatrix} + \Sigma_y(t) \begin{pmatrix} 0 & -i \\ i & 0 \end{pmatrix}, \quad (7)$$

in which $\Sigma_z(t) = (E_1 - E_2)/2$ and $\Sigma_y(t) = \hbar\mathcal{T}_{1,2}$ indicate the longitudinal and transversal components of an external driving field. Besides, the inset of Fig. 3(d) exhibits the specific time evolutions of $\Sigma_{y,z}(t)$ at $T_0 = 1.8$ and $w_0 = 6t_0$, with $\beta = 0.2\pi$. By contrast to the persistence of $\Sigma_z(t)$, it is seen that a considerable $\Sigma_y(t)$ can only exist around the zero time [see the inset of Fig. 3(d)]. Consequently, the TLS, as preset in the ground state ($|\Psi_1\rangle$) at $t = -w_0$, will undergo a transient oscillation. In accordance with the major component ($|l, \downarrow / \uparrow\rangle$) in $|\Psi_{1/2}(w_0)\rangle$, the mixing of the two basis states in its final state can be used to quantify the spin orientation of a transferred qubit. In addition, for $\beta \in [0, \pi/2]$ the spin-deviation angle ϑ_s can be approximated by the tilting degree of the driving field at the zero time

$$\vartheta_s \simeq \frac{2V_0\xi_0}{\sqrt{V_0^2\xi_0^2 + 4T_0^2\Sigma_z^2(0)w_0^2\cos^2\beta}}, \quad (8)$$

with $\xi_0 = \hbar\pi(\sqrt{\tau_1} + \sqrt{\tau_2})/2$ and $\tau_{1/2} = [1 \pm \cos(2\chi_1)][1 \mp \cos(2\chi_2)]$ at $\epsilon = 0$. The details are provided in Appendix B. It follows that the vanishing of ξ_0 at $\beta = 0$ prevents the spin deviation, and the upward trend of ϑ_s with β in Fig. 3(c) can be (roughly) explained by the presence of $\cos\beta$ in Eq. (8). Analogously, the difference from the local quantization axis is also expected to enlarge with the decline of T_0 or/and w_0 . However, a continuous reduction in these parameters will push the system beyond the viable operational regime for realizing high-fidelity inter-dot transfer [see Fig. 3(b)], a prerequisite for studying the deviation of a transferred qubit from the local spin axis. Given this constraint, it imposes a fundamental limit on the attainable magnitude of ϑ_s . For a fixed value of w_0 (or T_0), the maximum attainable value of ϑ_s can then be achieved as T_0 (or w_0) approaches the threshold boundary [see Fig. 3(d)].

Practically, w_0 and T_0 are the critical experimental parameters routinely tuned to control the spin state of a qubit following inter-dot transfer^{21,22,30}. Their specific values dictate whether the transfer process approaches the non-adiabatic or adiabatic regime. Here, by examining the evolution of qubit spin orientation across a range of parameter values, our study identifies an intriguing optimal parameter regime favorable for the implementation of shuttling-based qubit gates. This regime not only ensures high-fidelity transfer (i.e., $\mathcal{F}_c < 1\%$) but also guarantees a significant spin deviation (i.e., $\vartheta_s > 0.1\pi$), as highlighted by the double-headed arrow in Fig. 3(d). Evidently, this finding also enriches the research on non-adiabatic spin dynamics of a qubit shuttled between QDs with different Landé g -tensors.

Indeed, the spin states of a qubit before and after a high-fidelity inter-dot shuttling are interconnected by

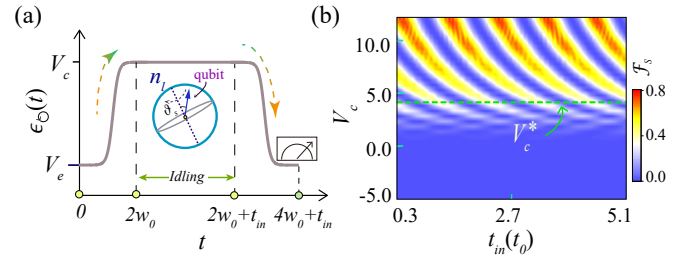


FIG. 4. (a) The time dependence of $\epsilon_{\text{O}}(t)$ to implement one round of inter-dot transfer, in which the up/down arrow indicates the leftward/rightward shuttling and t_{in} is the time of a qubit idling in the left QD. In addition, both the Larmor precession of qubit stay in the left QD and the detection of its spin flipping at the final moment are indicated. (b) The spin-flipping probability \mathcal{F}_s for an initial spin-down qubit as a function of t_{in} and V_c with $\varphi_{\text{so}} = 0.11\pi$, $\theta_r = 0.44\pi$, $\theta_l = 0.95\pi$, $V_e = -10$, $T_0 = 2.0$, $w_0 = 2t_0$, and V_c^* being the threshold of the plateau value (V_c) for completing inter-dot transfers.

a transfer matrix. More generally, the spin state of a qubit located in the left/right QD can be presented as $|\psi_{l/r}\rangle = \sum_{\sigma=\uparrow,\downarrow} \nu_{l/r,\sigma} |l/r, \sigma\rangle$, with $\nu_{\kappa=l,r} = \{\nu_{\kappa,\downarrow}, \nu_{\kappa,\uparrow}\}^T$ indicating the combination coefficients. The effect of a leftward/rightward shuttling is reflected by the relation $\nu_{l/r} = \hat{S}_{l/r} \nu_{r/l}$, with $\hat{S}_{\kappa=l,r}$ indicating the connection matrix. Besides the formation of spin deviation from the local quantization axis, it is important to notice that nonzero local Zeeman splitting can render spin-up and spin-down qubits to accumulate different dynamic phases, i.e., $\pm\phi_z$ with $\phi_z \propto g_0 w_0$ and $g_0 = \Delta_0/\hbar$, during the shuttling. Accordingly, \hat{S}_{κ} is shown to have the form of

$$\hat{S}_{\kappa} = \begin{pmatrix} e^{i\phi_{\kappa}} \cos \frac{\vartheta_s}{2} & -e^{-i\Theta_{\kappa}} \sin \frac{\vartheta_s}{2} \\ e^{i\Theta_{\kappa}} \sin \frac{\vartheta_s}{2} & e^{-i\phi_{\kappa}} \cos \frac{\vartheta_s}{2} \end{pmatrix}, \quad (9)$$

with $\phi_{\kappa=l/r} = \phi_z \pm (\phi_{\delta} - \phi_0)$, $\Theta_{\kappa} = \phi_{\kappa} + \varphi_{\kappa}$, and $\varphi_r = 2\phi_{\delta} + \phi_z + \pi$. Thus far, we have established a basic framework to fully capture the spin dynamic evolution of a transferred qubit undergoing non-adiabatic inter-dot shuttling. Building on this foundation, we are now poised to explore the practical implementation of shuttling-based spin qubit gates.

IV. IMPLEMENTATION OF SHUTTLING-BASED SPIN QUBIT GATES

In contrast to the unidirectional transport scheme reported in Ref. 40, the shuttling-based single-qubit gates are implemented by returning the qubit to its initial QD. Evidently, this design can effectively mitigate gate infidelity induced by spatial inhomogeneities in system parameters. For a semiconductor circuit composed of

two (or more) QDs, spin-qubit initialization and read-out can be conveniently realized by leveraging the Pauli spin blockade effect^{22,34}, which directly encodes the qubit spin state into a measurable charge signal. Interestingly, for an initial spin-polarized qubit, the deviation from the local quantization axis of one target QD can be manifested by its spin-flipping signal following a single round of inter-dot transfer³⁰.

Addressed concretely, the control of the time idling in the target QD is critical for determining the spin-flipping probability \mathcal{F}_s . For brevity, the detuning required to implement one round of anticlockwise inter-dot transfers is modulated as $\epsilon_{\circlearrowleft}(t) = V_e + V_a\{f_1(t)\tilde{H}(q_0 - t) + f_2(t)[1 - \tilde{H}(q_0 - t)]\}$, as seen in Fig. 4(a). Here, $f_{1/2}(t) = (\tanh[\pi(q_{1/2} \pm t)/w_0] + 1)/2$, $q_0 = 2w_0 + t_{in}$, $q_1 = -w_0$, $q_2 = 3w_0 + t_{in}$, $\tilde{H}(t)$ is the Heaviside function, and t_{in} represents the middle idling time. Correspondingly, Fig. 4(b) shows the spin-flipping probability \mathcal{F}_s for an initial spin-down qubit as a function of t_{in} and $V_c \equiv V_a + V_e$ at $t = t_{in} + 4w_0$. It is seen that \mathcal{F}_s can oscillate with t_{in} upon the completion of an inter-dot transfer, as indicated by $V_c > V_c^*$ in Fig. 4(b). In this case, the effect of leftward/rightward unidirectional shuttling can be captured by the respective connection matrix $\hat{S}_{l/r}$ in Eq. (9). Meanwhile, due to the presence of a nonzero local Zeeman splitting, a short stay in one target QD of t time can be mapped to an Z-gate operation $\hat{Z}(t) = \text{diag}\{e^{ig_0 t}, e^{-ig_0 t}\}$ ⁷⁴⁻⁷⁷. Then, the operation matrix for describing the one round of inter-dot transfer becomes $\mathbf{U}_{\circlearrowleft} = \hat{S}_r \hat{Z}(t_{in}) \hat{S}_l$, by which the flipping probability can be estimated as

$$\mathcal{F}_s = \sin^2 \vartheta_s \cos^2(\phi_d + g_0 t_{in}), \quad (10)$$

with $\phi_d = \phi_r + (\varphi_r - \varphi_l)/2$. Please refer to Appendix C for the detailed derivations. With the extension of t_{in} , it follows that the oscillation amplitude of \mathcal{F}_s can be used to quantify the deviation angle ϑ_s . Specifically, the raising of the amplitude with the increase of V_c in Fig. 4(b) can be principally illustrated by the positive dependence of ϑ_s on V_0 in Eq. (8). The concurrent tilting of the oscillating stripes is resulted from the variations in ϕ_d . In addition, the consistency with the detections in Fig. 2(b) of Ref. 30 validates our theoretical analyses.

Predictably, the Pauli-X and Pauli-Y gates for a single spin qubit are implemented along the flipping of its initial spin orientation, a condition that corresponds to $\mathcal{F}_s = 1$ in Eq. (10). While for the general scenario of $\vartheta_s \neq \pi/2$, the inequality $\mathcal{F}_s < 1$ precludes the realization of single-qubit gates by using the one-round inter-dot shuttling protocols. It should explore more rounds of inter-dot transfer processes to implement single-qubit gates in practical scenarios^{21,22}. For simplicity, herein the gates are assumed to be realized based on two-round bidirectional shuttling protocols. Explicitly, the time evolution of the desired detuning $\epsilon_{2\circlearrowleft}(t)$ to implement the protocols is displayed in Fig. 4(a), in which $t_{in/out,n=1,2}$ denotes the time of the qubit idling in the left/right QD in

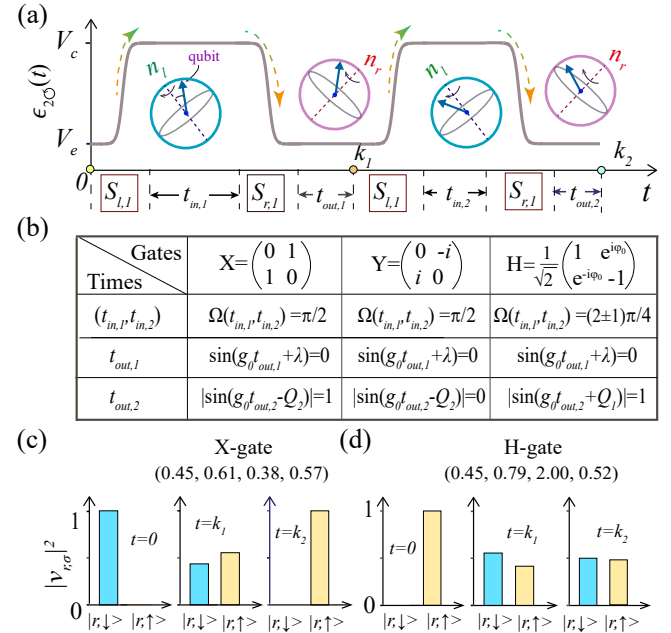


FIG. 5. (a) The modulation sequence of $\epsilon_{2\circlearrowleft}(t)$ to realize the two rounds of inter-dot shuttling protocol, in which $t_{in/out,n=1,2}$ indicates the time idling in the left/right QD and $\hat{S}_{l/r,n}$ represents the connection matrix of the leftward/rightward shuttling in the n -th round. Therein, $k_1 = 4w_0 + t_{in,1} + t_{out,1}$, $k_2 = 8w_0 + \sum_{n=1}^2 (t_{out,n} + t_{in,n})$, and the Larmor precessions of a qubit idling in the QDs are also indicated. (b) Explicit equations for determining the requisite idling times $t_{in,1}$, $t_{in,2}$, $t_{out,1}$ and $t_{out,2}$ to implement the single-qubit X, Y, and generalized Hadamard (H) gates. (c) and (d) In the implementation of the shuttling-based X and H gates, the composition ratios $|\nu_{r,\sigma}|^2$ of the local basis state $|r, \sigma\rangle$ in the evolving state of a spin-polarized qubit at $t = 0$ and $k_1,2$. Besides, the specific values of $(t_{in,1}, t_{out,1}, t_{in,2}, t_{out,2})$, in units of t_0 , are indicated in the panels and with the other parameters fixed as $\varphi_{so} = 0.11\pi$, $\theta_r = 0.44\pi$, $\theta_l = 0.95\pi$, $T_1 = 2.0$, $T_2 = 2.2$, $w_0 = 5t_0$, and $V_{c/e} = \pm 10$.

the n -th round. The concrete form of $\epsilon_{2\circlearrowleft}(t)$ can refer to Appendix C. Similar to Eq. (9), we can use $\hat{S}_{l/r,n}$ to represent the connection matrix of the leftward/rightward inter-dot shuttling in the n -th round. Meanwhile, due to the modulation in the corresponding tunnel-coupling strength T_n , the connection matrices of the two rounds are characterized by the distinct $\vartheta_{s,n}$, $\phi_{l/r,n}$, and $\varphi_{l/r,n}$, respectively. Besides, the specific values of these characteristic parameters are listed in Table I for different values of T_n and w_0 . Expressed in the local spin basis $\{|r, \downarrow\rangle, |r, \uparrow\rangle\}^T$ of the original QD, the overall operation matrix describing the effect of the shuttling protocol is then constructed as

$$\mathbf{U}_{2\circlearrowleft} = \hat{Z}(t_{out,2}) \hat{S}_{r,2} \hat{Z}(t_{in,2}) \hat{S}_{l,2} \hat{Z}(t_{out,1}) \cdot \hat{S}_{r,1} \hat{Z}(t_{in,1}) \hat{S}_{l,1}. \quad (11)$$

In accordance with the characteristics of the connection matrices $\hat{S}_{l/r,n}$, it is noted that a fine tuning of the idling times $t_{in,n}$ and $t_{out,n}$ is crucial to the implementation of the single-qubit gates, as exhibited in Fig. 5(b). To facilitate the analysis, two $t_{in,n}$ -dependent variables are introduced as $A_{n=1,2} = \cos \zeta_n \cos \vartheta_{s,n} + i \sin \zeta_n$, where $\zeta_n = g_0 t_{in,n} + \phi_{d,n}$ and $\phi_{d,n} = \phi_{r,n} - (\varphi_{l,n} - \varphi_{r,n})/2$. Then, the requirement for the time idling in the right QD in the first round can be reflected by the formula $\sin(g_0 t_{out,1} + \lambda) = 0$, with $\lambda = \eta_s + \phi_{l,2} - \varphi_{12,c}$, $\varphi_{nn',c/s} = (\varphi_{r,n} \mp \varphi_{l,n'})/2$, and $\eta_{c/s} = [\arg(A_1) \mp \arg(A_2)]/2$. Under this circumstance, the operation matrix in Eq. (11) can be further simplified into

$$\mathbf{U}_{2\circlearrowleft} = \begin{pmatrix} \cos \Omega e^{ig_0 t_{out,2} + iQ_1} & -\sin \Omega e^{ig_0 t_{out,2} - iQ_2} \\ \sin \Omega e^{-ig_0 t_{out,2} + iQ_2} & \cos \Omega e^{-ig_0 t_{out,2} - iQ_1} \end{pmatrix}, \quad (12)$$

in which $\Omega(t_{in,1}, t_{in,2}) = \sum_n \arccos |A_n|$ and $Q_{1/2} = \eta_{s/c} \mp \varphi_{21,c/s} + \phi_{l,1}$. It is evident that the single-qubit Pauli-X gate can be attained if $(t_{in,1}, t_{in,2})$ satisfy the condition of $\Omega = \pi/2$ and $|\sin(g_0 t_{out,2} - Q_2)| = 1$. Furthermore, the Pauli-Y gate is obtained by adjusting $t_{out,2}$ to meet the corresponding condition $|\sin(g_0 t_{out,2} - Q_2)| = 0$. Interestingly, a generalized Hadamard (H) gate in Fig. 5(b) can also be realized when $\Omega = (2 \pm 1)\pi/4$ and $|\sin(g_0 t_{out,2} + Q_1)| = 1$, where the off-diagonal phase shift is estimated as $\varphi_o = \tilde{\varphi} \mp \pi/2$ with $\tilde{\varphi} = \pi/2 - Q_1 - Q_2$. The detailed derivations are presented in Appendix C.

For a qubit initialized in the spin-down state of the right QD at $t = 0$, Fig. 5(c) shows the variations in the composition ratio $|\nu_{r,\uparrow/\downarrow}|^2$ of the local basis state $|r, \uparrow/\downarrow\rangle$ in the qubit evolving state at $t = k_1$ and $t = k_2$. These two time points correspond to the completion of the first and second rounds of inter-dot transfer, respectively. Equipped with a precise control of the idling times $(t_{in,1}, t_{in,2}, t_{out,1}, t_{out,2})$, it is seen that the spin orientation of the qubit is reversed, i.e., $\nu_{r,\downarrow}(k_2) = 0$ and $|\nu_{r,\uparrow}(k_2)|^2 = 1$, after going through the X-gate modulation. In addition, Fig. 5(d) illustrates that a generalized H gate can also be attained with tuning $t_{out,1}$, $t_{in,1}$, and $t_{out,2}$. For a qubit initialized in the spin-up state of the right QD, the composition ratios are found to be equal in the final state, i.e., $\nu_{r,\uparrow/\downarrow}(k_2) = 1/2$, and a qubit superposition state of the form $(e^{i\varphi_0}|r, \downarrow\rangle - |r, \uparrow\rangle)/\sqrt{2}$ is thus generated following the H-gate control sequence.

V. DISCUSSION AND CONCLUSION

To date, the effect of spin decoherence have been neglected in the theoretical modeling of shuttling-based single-qubit gates. Indeed, this simplification is well-founded on the basis of a long coherence time of the spin qubit. For instance, the coherence times of a hole spin qubit in the Ge-based QDs in Ref. 22 have reached to a few of microseconds. By contrast, the ramping time of the detuning in experiments is on the order of nanoseconds^{21,22,30}, far less than the scale of the coherence time. Thus, the spin qubit can maintain excellent coherence during multiple rounds of inter-dot transfer for realizing qubit gates. Especially, a significant deviation of the transferred qubit from the spin-quantization axis of its residing QD is critical to the design of shuttling-based single-qubit gates. For the case of $\vartheta_{s,n=1,2} < \pi/4$, the inequality $\Omega(t_{in,1}, t_{in,2}) \neq \pi/2$ excludes the implementation of the X and Y gates using the two rounds of inter-dot shuttling protocol. In such cases, it should explore more rounds of inter-dot transfer to realizing the anticipated logic gates, but a short and brief modulation protocol is much preferable to experiments.

Accordingly, in this work, we thoroughly study the change in the spin orientation of a qubit after undergoing a non-adiabatic shuttling between two QDs with different spin quantization axes. With the realization of a high-fidelity inter-dot transfer, we reveal that the deviation from the local spin quantization axis is controllable, and can be effectively regulated by the tunnel-coupling strength and the ramping time of the detuning. In addition, based on the characteristics of two rounds of the designed inter-dot shuttling, we estimate the requisite idling times for realizing the single-qubit X, Y and generalized Hadamard gates. Overall, we believe our study will invoke more interest regarding the non-adiabatic control of the spin orientation of a transferred qubit and the implementation of high-fidelity shuttling-based quantum logic gates in semiconductor QD arrays.

Acknowledgements— This work is supported by the National Natural Science Foundation of China (Grants No. 92565304 and No. 92165208). X.-F. Liu acknowledges support from the National Natural Science Foundation of China (Grant No. 62501059) and the National Key Research and Development Program of China (Grant No. 2025YFE0217400).

Appendix A: The derivation of the spin-dependent tunneling amplitudes

In this Appendix, we outline the calculation procedures for determining the spin-dependent amplitudes for a spin qubit tunneling between two QDs with different spin-quantization axes. In addition, the constraints on the magnetic-field magnitude B for defining well-behaved spin qubits in QDs and the analytic forms of the higher-energy states $|\Psi_{3,4}\rangle$ are presented.

In the presence of an external magnetic field applied in the y direction [see Fig. 1(a)], the distinct spin states of a

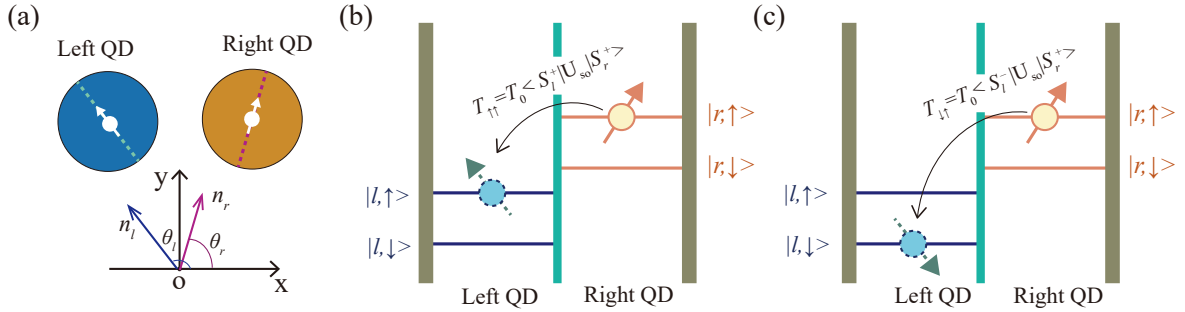


FIG. 6. (a) Schematic of the spin-quantization axes of the left and right QDs, i.e., $\hat{n}_l = (\cos \theta_l, \sin \theta_l, 0)$ and $\hat{n}_r = (\cos \theta_r, \sin \theta_r, 0)$, in the $x - y$ plane. (b) The “spin-conserved” tunneling of a qubit between the upper Zeeman splitting states $|l, \uparrow\rangle$ and $|r, \uparrow\rangle$ of the two QDs, with $T_{\uparrow, \uparrow}$ indicating the tunneling amplitude. (c) The “spin-flipped” tunneling for a qubit transferring from the spin-up state $|r, \uparrow\rangle$ of the right QD to the spin-down state $|l, \downarrow\rangle$ of the other QD and with $T_{\downarrow, \uparrow}$ denoting the amplitude.

single hole (or electron) confined in the QDs undergo splitting due to the Zeeman effect. Before proceeding further, the introduction of well-defined spin qubits in QDs actually imposes strict constraints on the field magnitude B . To begin with, the magnetic-field induced Zeeman splitting Δ_z must be smaller than the QD orbital energy-level splitting ΔE_{orb} , a fundamental condition for ensuring the encoding of pure spin qubits. For a qubit of $\Delta E_{\text{orb}} \sim 1.2\text{meV}$; with $g \simeq 0.4$ for Ge holes⁴⁴, the corresponding upper threshold for B is 51 T [calculated via $B = \Delta E_{\text{orb}} / (g\mu_B)$]. In addition, accounting for the hyperfine interaction with nuclear spins, the magnitude B should be much larger than the strength (B_{hf}) of the average hyperfine fields for mitigating its adverse impacts^{55–57}. Furthermore, when considering the inverse- B dependence of spin qubit relaxation times, the preservation of long qubit coherence times also impose an upper limit on the value of B ^{78–81}. For instance, the coherence times of Ge-based hole spin qubits in experiments can reach to the microsecond regime as $B \leq 40\text{ mT}$ (while exceeding $B_{hf} \sim 20\mu\text{T}$)²², and this prolonged coherence window effectively suppresses the formation of relaxation-induced unintended spin polarization in subsequent qubit manipulations.

With including both the spin and spatial degrees of freedom, the low-energy Zeeman splitting states of the qubit in the QDs can be formulated as

$$|l/r, \uparrow\rangle = \psi_0(x \pm d, y) |s_{l/r}^+\rangle \quad |l/r, \downarrow\rangle = \psi_0(x \pm d, y) |s_{l/r}^-\rangle. \quad (\text{A1})$$

Here, $\psi_0(x \pm d, y)$ indicates the ground-state wavefunction of the left/right QD in the $x - y$ plane, $2d$ quantities the inter-dot distance along the x direction, and $|s_{l/r}^\pm\rangle$ characterize the spin components. Because of the inhomogeneity in the Landé g -tensor, the orientation of their spin quantization axis is different between the left and right QDs, just as shown in Fig. 6(a). More specifically, the local spin components in Eq. (A1) satisfy the relation $(\hat{n}_\kappa \cdot \boldsymbol{\sigma}) |s_\kappa^\pm\rangle = \pm |s_\kappa^\pm\rangle$ and, expanded in the unified spin basis of $\{| \uparrow \rangle, | \downarrow \rangle\}^T$ with $\sigma_z | \uparrow \rangle / | \downarrow \rangle = \pm | \uparrow \rangle / | \downarrow \rangle$, they can be written as

$$|s_\kappa^+\rangle = \frac{1}{\sqrt{2}} \begin{pmatrix} \cos \frac{\theta_\kappa}{2} - i \sin \frac{\theta_\kappa}{2} \\ \cos \frac{\theta_\kappa}{2} + i \sin \frac{\theta_\kappa}{2} \end{pmatrix} \quad |s_\kappa^-\rangle = \frac{1}{\sqrt{2}} \begin{pmatrix} i \sin \frac{\theta_\kappa}{2} - \cos \frac{\theta_\kappa}{2} \\ \cos \frac{\theta_\kappa}{2} + i \sin \frac{\theta_\kappa}{2} \end{pmatrix}. \quad (\text{A2})$$

Theoretically, the strength of tunnel-coupling between two coupled QDs, denoted by T_0 , is correlated to the overlap between the qubit’s spatial wave-functions $\psi_0(x \pm d, y)$ ⁸². In experiments, this can be regulated by the middle barrier-gate potential⁸³, see V_M in Fig. 1(a). Given the difference in the spin-quantization axes of the coupled QDs, the spin-dependent tunneling amplitude $T_{\sigma', \sigma}$ depends not only on the tunnel-coupling strength, but also on the disparity in the spin axes of the two QDs. Beyond these factors, it can also be regulated by the SOI in the semiconductors. Specifically, the Hamiltonian for the (linear) Rashba SOI along the tunneling (x -axis) direction takes the form of $H_{\text{so}} = \alpha_{\text{so}} p_x \sigma_y$ ⁸⁴, where $p_x = -i\hbar\partial/(\partial x)$ and α_{so} denotes the strength of the SOI. In conjunction with inter-dot tunneling, the SOI effect behaves as a unitary operator acting on the transferred spin qubit⁸⁵

$$\mathbf{U}_{\text{so}} = \exp(i\varphi_{\text{so}} \sigma_y) = \begin{pmatrix} \cos \varphi_{\text{so}} & \sin \varphi_{\text{so}} \\ -\sin \varphi_{\text{so}} & \cos \varphi_{\text{so}} \end{pmatrix}. \quad (\text{A3})$$

Here, $\varphi_{\text{so}} = 2d/\ell_{\text{so}}$ indicates the Aharonov-Casher (AC) phase, $\ell_{\text{so}} = \hbar/(m_e \alpha_{\text{so}})$ is the effective spin-orbit length, and m_e the effective mass of the charged particle. Then, the amplitude for a qubit tunneling from the upper/lower

Zeeman-splitting state of the right QD to the upper/lower splitting state of the left QD can be evaluated as $T_{\uparrow\uparrow/\downarrow\downarrow} = T_0 \langle s_l^\pm | \mathbf{U}_{\text{so}} | s_r^\pm \rangle$, see Fig. 6(b). Based on Eqs. (A2) and (A3), it can be further simplified into

$$T_{\uparrow\uparrow/\downarrow\downarrow} = T_0 \left(\cos \varphi_{\text{so}} \cos \frac{\theta_r - \theta_l}{2} \pm i \sin \varphi_{\text{so}} \sin \frac{\theta_r + \theta_l}{2} \right). \quad (\text{A4})$$

with $\theta_\delta = (\theta_r - \theta_l)/2$ and $\theta_0 = (\theta_r + \theta_l)/2$. Analogously, the amplitude for a qubit tunneling from the lower/upper Zeeman-splitting state of the right QD to the upper/lower splitting state of the other QD is give by $T_{\uparrow\downarrow/\downarrow\uparrow} = T_0 \langle s_l^\pm | \mathbf{U}_{\text{so}} | s_r^\mp \rangle$, see Fig. 6(c). According to the concrete expressions of the spin components in Eq. (A2), these amplitudes can be calculated as

$$T_{\uparrow\downarrow/\downarrow\uparrow} = T_0 \left(i \cos \varphi_{\text{so}} \sin \frac{\theta_r - \theta_l}{2} \pm \sin \varphi_{\text{so}} \cos \frac{\theta_r + \theta_l}{2} \right). \quad (\text{A5})$$

By including the influence of inter-dot detuning (ϵ), the effective Hamiltonian describing the single qubit in the double QDs is given in Eq. (1). To facilitate the analysis, the spin-dependent tunneling amplitudes in Eqs. (A4) and (A5) are reformulated as

$$\begin{aligned} T_{\uparrow\uparrow} &= T_0 \cos \beta e^{i\tilde{\zeta}_1} & T_{\downarrow\downarrow} &= T_0 \cos \beta e^{-i\tilde{\zeta}_1} \\ T_{\uparrow\downarrow} &= T_0 \sin \beta e^{i\tilde{\zeta}_2} & T_{\downarrow\uparrow} &= -T_0 \sin \beta e^{-i\tilde{\zeta}_2}, \end{aligned} \quad (\text{A6})$$

with $\beta = \arccos(|T_{\uparrow\uparrow}|/T_0)$, $\tilde{\zeta}_1 = \arg(T_{\uparrow\uparrow})$, and $\tilde{\zeta}_2 = \arg(T_{\uparrow\downarrow})$. Based on this, a new normalized local basis $\mathbf{\Pi} = \{e^{i\phi_0}|l,\uparrow\rangle, e^{-i\phi_0}|l,\downarrow\rangle, e^{i\phi_\delta}|r,\uparrow\rangle, e^{-i\phi_\delta}|r,\downarrow\rangle\}^T$ is introduced, with $\phi_{0/\delta} = (\tilde{\zeta}_2 \pm \tilde{\zeta}_1)/2$. By projecting into the new basis, the Hamiltonian in Eq. (1) can be expanded as

$$H_0(\epsilon) = \begin{pmatrix} E_{l\uparrow} & 0 & T_0 \cos \beta & T_0 \sin \beta \\ 0 & E_{l\downarrow} & -T_0 \sin \beta & T_0 \cos \beta \\ T_0 \cos \beta & -T_0 \sin \beta & E_{r\uparrow} & 0 \\ T_0 \sin \beta & T_0 \cos \beta & 0 & E_{r\downarrow} \end{pmatrix}. \quad (\text{A7})$$

Then, the energies $E_{j=1-4}$ of the single qubit can be analytically derived through the direct diagonalization of Eq. (A7), i.e.,

$$\begin{aligned} E_1(\epsilon) &= -\sqrt{(\Delta_0 + \Gamma_0)^2 + T_0^2 \sin^2 \beta} & E_2(\epsilon) &= -\sqrt{(\Delta_0 - \Gamma_0)^2 + T_0^2 \sin^2 \beta} \\ E_3(\epsilon) &= \sqrt{(\Delta_0 - \Gamma_0)^2 + T_0^2 \sin^2 \beta} & E_4(\epsilon) &= \sqrt{(\Delta_0 + \Gamma_0)^2 + T_0^2 \sin^2 \beta}, \end{aligned} \quad (\text{A8})$$

with $\Delta_0 = \Delta_z/2$ and $\Gamma_0 = \sqrt{\epsilon^2 + T_0^2 \cos^2 \beta}$. In accordance with the corresponding eigenvectors, the lowest two energy states $|\Psi_{1,2}\rangle$ are given in Eq. (3) of the main text. Similarly, the specific forms of the two higher-energy states $|\Psi_{3,4}(\epsilon)\rangle$ are presented by

$$|\Psi_3(\epsilon)\rangle = \begin{pmatrix} \cos \alpha \cos \chi_2 \\ \sin \alpha \sin \chi_2 \\ -\sin \alpha \cos \chi_2 \\ \cos \alpha \sin \chi_2 \end{pmatrix} \quad |\Psi_4(\epsilon)\rangle = \begin{pmatrix} \sin \alpha \sin \chi_1 \\ -\cos \alpha \cos \chi_1 \\ \cos \alpha \sin \chi_1 \\ \sin \alpha \cos \chi_1 \end{pmatrix}, \quad (\text{A9})$$

with the specific expressions of α and $\chi_{n=1,2}$ illustrated in the main text below Eq. (3).

Appendix B: The analytic expressions of the matrix elements $\mathcal{T}_{j,j'}(t)$

In this Appendix, we outline the specific expressions of the matrix elements $\mathcal{T}_{j,j'}(t)$ in Eq. (4). Besides, the derivation of the analytical approximation for the spin derivation angle in Eq. (8) is presented.

According to the orthogonality of the energy states $|\Psi_{j=1-4}(\epsilon)\rangle$, the time evolution state of the qubit can be expanded as $\Phi(t) = \sum_{j=1}^4 C_j(t) |\Psi_j(\epsilon)\rangle$. Substituting it into the time-dependent Schrödinger equation

$$i\hbar \frac{\partial}{\partial t} \Phi(t) = H_0(\epsilon) \Phi(t), \quad (\text{B1})$$

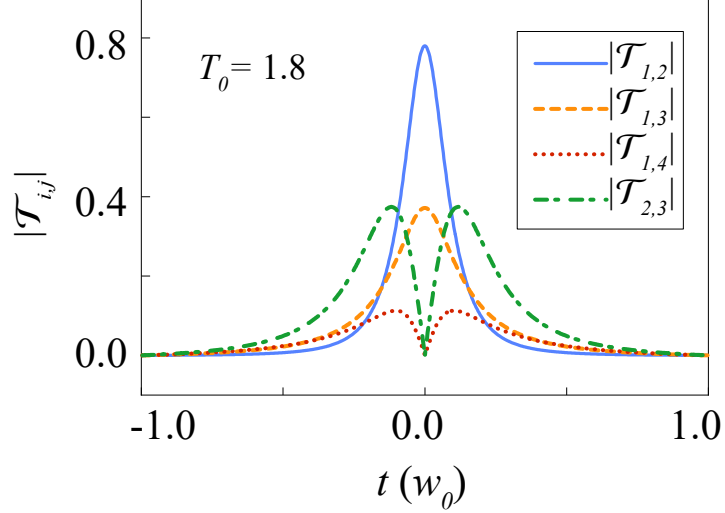


FIG. 7. (a) The magnitudes of the transition elements $|\mathcal{T}_{1,2}|$, $|\mathcal{T}_{1,3}|$, $|\mathcal{T}_{1,4}|$, and $|\mathcal{T}_{2,3}|$ (in units of π/t_0) as a function of t with $T_0 = 1.8$, $V_0 = 10$, $\beta = 0.32\pi$, and $w_0 = 6t_0$.

it is found that the combinational coefficients $C_j(t)$ are determined by the the differential equation (4) of the main text

$$i\frac{dC_j(t)}{dt} + i\sum_{j'=1}^4 \mathcal{T}_{j,j'}(t)C_{j'}(t) = \frac{E_j(\epsilon)}{\hbar}C_j(t) , \quad (\text{B2})$$

with $\mathcal{T}_{j,j'}(t) = \langle \Psi_j(\epsilon) | \partial_t | \Psi_{j'}(\epsilon) \rangle$. Based on the concrete form of $|\Psi_j\rangle$ in Eqs. (3) and (A9), it is found that $\mathcal{T}_{j,j'}(t) = -\mathcal{T}_{j',j}(t)$ as such the off-diagonal terms $\mathcal{T}_{j,j} = 0$. The off-diagonal terms are derived by

$$\begin{aligned} \mathcal{T}_{1,2}(t) &= -\mathcal{T}_{2,1}(t) = \sin(\chi_1 + \chi_2) \frac{\partial\alpha}{\partial t} \\ \mathcal{T}_{1,3}(t) &= -\mathcal{T}_{3,1}(t) = -\cos(\chi_1 + \chi_2) \frac{\partial\alpha}{\partial t} \\ \mathcal{T}_{1,4}(t) &= -\mathcal{T}_{4,1}(t) = \frac{\partial\chi_1}{\partial t} \\ \mathcal{T}_{2,3}(t) &= -\mathcal{T}_{3,2}(t) = \frac{\partial\chi_2}{\partial t} \\ \mathcal{T}_{2,4}(t) &= -\mathcal{T}_{4,2}(t) = \cos(\chi_1 + \chi_2) \frac{\partial\alpha}{\partial t} \\ \mathcal{T}_{3,4}(t) &= -\mathcal{T}_{4,3}(t) = \sin(\chi_1 + \chi_2) \frac{\partial\alpha}{\partial t} . \end{aligned} \quad (\text{B3})$$

Based on the time-dependent modulation of the detuning $\epsilon(t) = V_0 \tanh(\pi t/w_0)$, and using the definitions of the specific parameters α and $\chi_{1,2}$, one can be obtain that

$$\begin{aligned} \frac{\partial\alpha}{\partial t} &= -\frac{\pi}{2} \frac{T_0 V_0 \cos \beta}{\Gamma_0^2 w_0} \operatorname{sech}^2\left(\frac{\pi t}{w_0}\right) \\ \frac{\partial\chi_n}{\partial t} &= \frac{\pi}{2} \frac{V_0^2 T_0 \sin \beta}{w_0 \Gamma_0 E_n^2} \operatorname{sech}^2\left(\frac{\pi t}{w_0}\right) \tanh\left(\frac{\pi t}{w_0}\right) . \end{aligned} \quad (\text{B4})$$

Accordingly, it is confirmed that $\mathcal{T}_{j',j} \propto \operatorname{sech}^2\left(\frac{\pi t}{w_0}\right)$, and Fig. 7 exhibits the specific time evolutions of $|\mathcal{T}_{1,2}|$, $|\mathcal{T}_{1,3}|$, $|\mathcal{T}_{1,4}|$ and $|\mathcal{T}_{2,3}|$. It can be observed that non-negligible nonzero values of $|\mathcal{T}_{1,2}|$ and $|\mathcal{T}_{1,3}|$ arise only near $t = 0$, where $|\mathcal{T}_{1,4}|$ and $|\mathcal{T}_{2,3}|$ simultaneously drop to zero owing to the factor $\tanh\left(\frac{\pi t}{w_0}\right)$ in the second line of Eq. (B4) .

Upon the realization of high-fidelity inter-dot transfer, it is demonstrated that the magnitudes of $|C_{3,4}|^2$ are significantly suppressed throughout the process, see Fig. 2(d) of the main text. Building on this result and in accordance with Eq. (B2), the time evolutions of $C_{1,2}$ can be captured by a simplified matrix equation

$$\frac{\partial}{\partial t} \begin{pmatrix} C_1(t) \\ C_2(t) \end{pmatrix} + \begin{pmatrix} 0 & \mathcal{T}_{1,2}(t) \\ \mathcal{T}_{2,1}(t) & 0 \end{pmatrix} \begin{pmatrix} C_1(t) \\ C_2(t) \end{pmatrix} = \frac{1}{i\hbar} \begin{pmatrix} E_1(t)C_1(t) \\ E_2(t)C_2(t) \end{pmatrix}. \quad (\text{B5})$$

Intriguingly, Eq. (B5) is found to be equivalent to the time-dependent Schrödinger equation for a two-level system (TLS) under an external driving field. Working in the 2D lower-energy state subspace $\{|\Psi_1(\epsilon)\rangle, |\Psi_2(\epsilon)\rangle\}^T$, to be more specific, the effective Hamiltonian is given by Eq. (7) of the main text, i.e.,

$$H_{\text{eff}}(t) = \Sigma_z(t) \begin{pmatrix} 1 & 0 \\ 0 & -1 \end{pmatrix} + \Sigma_y(y) \begin{pmatrix} 0 & -i \\ i & 0 \end{pmatrix}, \quad (\text{B6})$$

with $\Sigma_z(t) = (E_1 - E_2)/2$ and $\Sigma_y(t) = \hbar\mathcal{T}_{1,2}(t)$ indicating the longitudinal and transverse components of the driving field. Using Eqs. (B3) and (B4), the transverse component can be further evaluated as

$$\begin{aligned} \Sigma_y(t) = & -\frac{\pi}{4} \frac{\hbar V_0 T_0}{w_0 \Gamma_0^2(t)} \cos \beta \operatorname{sech}^2\left(\frac{\pi t}{w_0}\right) \left\{ \sqrt{[1 + \cos(2\chi_1)][1 - \cos(2\chi_2)]} \right. \\ & \left. + \sqrt{[1 - \cos(2\chi_1)][1 + \cos(2\chi_2)]} \right\}. \end{aligned} \quad (\text{B7})$$

As shown in the inset of Fig. 3(d) in the main text, Σ_y and Σ_z exhibit distinct time dependences. In contrast to the longitudinal component Σ_z , it is seen that the presence of a non-negligible transverse component $\Sigma_y(t)$ is confined to the vicinity of $t = 0$. This time-dependent behavior accounts for the deviation of a leftward transferred qubit from the local spin quantization axis. For a qubit initialized in the spin-down state of the right QD, it is confirmed that the deviation angle can be approximated by the tilting degree of the field at the central time, i.e., $\vartheta_s \simeq 2\Sigma_y(0)/\sqrt{\Sigma_z^2(0) + \Sigma_y^2(0)}$. Using the concrete form of $\Sigma_y(t)$ in Eq. (B7), it can be further simplified into Eq. (8) of the main text

$$\vartheta_s \simeq \frac{2V_0\xi_0}{\sqrt{V_0^2\xi_0^2 + 4T_0^2w_0^2\Sigma_z^2(0)\cos^2\beta}}, \quad (\text{B8})$$

in which $\xi_0 = \hbar\pi(\sqrt{\iota_1} + \sqrt{\iota_2})/2$ and $\iota_{1/2}$ denote the values of $[1 \pm \cos(2\chi_1)][1 \mp \cos(2\chi_2)]$ evaluated at $t = 0$, respectively. In the case of $\beta = 0$, it is found that $\vartheta_s = 0$ because $\iota_{n=1,2} = 0$. For $\beta \neq 0$ (or $\pi/2$), the spin deviation angle ϑ_s is dependent on the specific values of T_0 and w_0 , as discussed in the main text.

Appendix C: The requisite idling times in realizing single-qubit gates

In this Appendix, we present the details for ascertaining the required idling times in realizing the single-qubit X, Y, and generalized H gates. Before that, we outline the calculation process for determining the spin-flipping probability \mathcal{F}_s of a spin qubit after undergoing one round of inter-dot transfer.

Based on the explicit form of the connection matrix $\hat{S}_{l/r}$ given in Eq. (9) of the main text, the operation matrix describing one round of inter-dot transfer—driven by the time-dependent detuning modulation ϵ shown in Fig. 4(a)—can be expanded as

$$\mathbf{U}_{\mathcal{O}} = \hat{S}_r \hat{Z}(t_{in}) \hat{S}_l = \begin{pmatrix} e^{i\phi_l} M_{11} & e^{-i\phi_l} M_{12} \\ e^{i\phi_l} M_{21} & e^{-i\phi_l} M_{22} \end{pmatrix}, \quad (\text{C1})$$

in which

$$\begin{aligned} M_{11} = & e^{i\varphi_\delta} [\cos(g_0 t_{in} + \phi_d) \cos \vartheta_s + i \sin(g_0 t_{in} + \phi_d)] \\ M_{12} = & -e^{-i\varphi_0} \sin \vartheta_s \cos(\phi_d + g_0 t_{in}), \end{aligned} \quad (\text{C2})$$

$M_{22} = M_{11}^*$, and $M_{21} = -M_{12}^*$, with $\varphi_{0/\delta} = (\varphi_l \pm \varphi_r)/2$ and $\phi_d = \phi_r - \varphi_\delta$. Expressed in the local spin basis $\{|r, \downarrow\rangle, |r, \uparrow\rangle\}^T$, the evolved spin state of a qubit initialized in the spin-down state of the right QD at $t = 0$ can then be calculated as

$$|\psi_r(t_f)\rangle = \mathbf{U}_{\mathcal{O}} \begin{pmatrix} 1 \\ 0 \end{pmatrix} = \begin{pmatrix} e^{i\phi_l} M_{11} \\ e^{i\phi_l} M_{21} \end{pmatrix}, \quad (\text{C3})$$

TABLE I. The characteristic parameters of the connection matrix in Eq. (C7), i.e., $\vartheta_{s,n}$, $\varphi_{l,n}$, $\varphi_{r,n}$, $\phi_{l,n}$, and $\phi_{r,n}$, with $V_{c/e} = \pm 10$ (in a unit of Δ_0) and different values of T_n and w_0 . Besides, in the specific modulations, the direction angles of the QDs' spin quantization are set as $\theta_l = 0.95\pi$ and $\theta_r = 0.44\pi$ and the SOI-induced rotation phase is $\phi_{so} = 0.11\pi$.

w_0	T_1	$\vartheta_{s,1}$	$\varphi_{l,1}$	$\varphi_{r,1}$	$\phi_{l,1}$	$\phi_{r,1}$	T_2	$\vartheta_{s,2}$	$\varphi_{l,2}$	$\varphi_{r,2}$	$\phi_{l,2}$	$\phi_{r,2}$
$5t_0$	2.00	0.28π	1.00π	1.76π	0.08π	0.32π	2.20	0.25π	1.05π	1.80π	0.04π	0.28π
$6t_0$	1.80	0.27π	1.05π	1.80π	0.04π	0.28π	2.00	0.24π	1.09π	1.84π	0.00	0.24π

with $t_f = 4w_0 + t_{in}$. Consequently, it follows that the spin-flipping probability \mathcal{F}_s of the transferred qubit can be estimated as

$$\mathcal{F}_s = |\mathbf{M}_{21}|^2 = \sin^2 \vartheta_s \cos^2(\phi_d + g_0 t_{in}) . \quad (\text{C4})$$

For the general case of $\vartheta_s \neq 0$, it is evident that the implementation of the single-qubit Pauli-X and Pauli-Y gates necessitates multiple rounds of inter-dot transfer. To simplify the analysis, the explicit time-dependent detuning used to induce two rounds of inter-dot transfer is modulated as

$$\epsilon_{2\circlearrowleft}(t) = V_e + V_a \sum_{n=1,2} \Upsilon_n(t) , \quad (\text{C5})$$

with

$$\Upsilon_n(t) = J_n(t - w_0) \tilde{H}(t - \varsigma_{n,1}) [1 - \tilde{H}(t - \varsigma'_{n,1})] + J_n(z_n + w_0 - t) \tilde{H}(t - \varsigma_{n,2}) [1 - \tilde{H}(t - \varsigma'_{n,2})] . \quad (\text{C6})$$

Specifically, we define the following functions and parameters herein : $J_1(t) = [\tanh(\pi t/w_0) + 1]/2$, $J_2(t) = \{\tanh[\pi(t - k_1)/w_0] + 1\}/2$, $k_1 = 4w_0 + t_{in,1} + t_{out,1}$, $k_2 = 8w_0 + \sum_{n=1,2} (t_{in,n} + t_{out,n})$, $\varsigma_{1,1} = 0$, $\varsigma_{2,1} = k_1$, $\varsigma'_{n,1} = \varsigma_{n,2} = z_n$, and $\varsigma'_{n,2} = k_n$, in which $z_1 = 2w_0 + t_{in,1}$, $z_2 = k_1 + 2w_0 + t_{in,2}$, $t_{in/out,n}$ indicate the respective idling times within the left and right QDs , and $\tilde{H}(t)$ represents the Heaviside function. The time evolution of $\epsilon_{2\circlearrowleft}(t)$ is exhibited in Fig. 5(a) of the main text. In addition, the difference between the baseline value (V_e) and the plateau value ($V_c = V_e + V_a$) of the modulated detuning is set sufficiently large to ensure high-fidelity inter-dot transfer during each unidirectional shuttling process. By analogy with Eq. (9) of the main text, the connection matrix for describing the leftward/rightward transfer in the n -th round can then be presented as

$$\hat{S}_{l/r,n} = \begin{pmatrix} e^{i\phi_{l/r,n}} \cos \frac{\vartheta_{s,n}}{2} & -e^{-i\varphi_{l/r,n} - i\phi_{l/r,n}} \sin \frac{\vartheta_{s,n}}{2} \\ e^{i\varphi_{l/r,n} + i\phi_{l/r,n}} \sin \frac{\vartheta_{s,n}}{2} & e^{-i\phi_{l/r,n}} \cos \frac{\vartheta_{s,n}}{2} \end{pmatrix} . \quad (\text{C7})$$

Considering the modulation in the tunnel-coupling strength given by $T_0 = \begin{cases} T_1 & t \leq k_1 \\ T_2 & t > k_1 \end{cases}$, it can be inferred that the characteristic parameters of the connection matrix, namely $\vartheta_{s,n}$, $\varphi_{l/r,n}$, and $\phi_{l/r,n}$, exhibit distinct values between the first and second transfer rounds. Specifically, the distinct values of these basic characteristic parameters, corresponding to the different values of w_0 and T_n ($n = 1, 2$), are listed in Table I.

By incorporating the effect of short stays in the QDs, which corresponds to the Z-gate operations, the overall evolution matrix for describing the two rounds of inter-dot shuttling protocol is given by Eq. (11) of the main text. To facilitate the analysis, the operation matrix can be reformulated as

$$\mathbf{U}_{2\circlearrowleft} = \hat{Z}(t_{out,2}) \widehat{\text{Tw}}_2(t_{in,2}) \hat{Z}(t_{out,1}) \widehat{\text{Tw}}_1(t_{in,1}) , \quad (\text{C8})$$

with $\widehat{\text{Tw}}_n(t_{in,n}) = \hat{S}_{r,n} \hat{Z}(t_{in,n}) \hat{S}_{l,n}$. By analogy with Eq. (C1), it is found that

$$\widehat{\text{Tw}}_n(t_{in,n}) = \begin{pmatrix} e^{i\phi_{l,n}} \mathbf{M}_{11,n} & e^{-i\phi_{l,n}} \mathbf{M}_{12,n} \\ e^{i\phi_{l,n}} \mathbf{M}_{21,n} & e^{-i\phi_{l,n}} \mathbf{M}_{22,n} \end{pmatrix} , \quad (\text{C9})$$

in which the matrix elements are evaluated as

$$\begin{aligned} \mathbf{M}_{11,n} &= e^{i\varphi_{\delta,n}} [\cos \zeta_n \cos \vartheta_{s,n} + i \sin \zeta_n] \\ \mathbf{M}_{12,n} &= -e^{-i\varphi_{0,n}} \sin \vartheta_{s,n} \cos \zeta_n . \end{aligned} \quad (\text{C10})$$

with $\zeta_n = g_0 t_{in,n} + \phi_{d,n}$, $\varphi_{\delta,n} = (\varphi_{l,n} - \varphi_{r,n})/2$ and $\phi_{d,n} = \phi_{r,n} - (\varphi_{l,n} - \varphi_{r,n})/2$. Substituting Eq. (C9) into Eq. (C8) and by introducing two auxiliaries $A_n(t_{in,n}) = \cos \zeta_n \cos \vartheta_{s,n} + i \sin \zeta_n$, the evolution matrix can be derived as

$$\mathbf{U}_{2\circlearrowleft} = \begin{pmatrix} \Sigma T_1 & -\Sigma T_2 \\ \Sigma T_2^* & \Sigma T_1^* \end{pmatrix}, \quad (C11)$$

in which the matrix elements are calculated as

$$\begin{aligned} \Sigma T_1 &= e^{ig_0 t_{out,2} + iQ_1} [e^{ig_0 t_{out,1} + i\lambda} \cos \omega_1 \cos \omega_2 - e^{-ig_0 t_{out,1} - i\lambda} \sin \omega_1 \sin \omega_2] \\ \Sigma T_2 &= e^{ig_0 t_{out,2} - iQ_2} [e^{ig_0 t_{out,1} + i\lambda} \sin \omega_1 \cos \omega_2 + e^{-ig_0 t_{out,1} - i\lambda} \cos \omega_1 \sin \omega_2]. \end{aligned} \quad (C12)$$

Here $\omega_{n=1,2} = \arccos [|A_n(t_{in,n})|]$, $Q_{1/2} = \eta_{s/c} \mp \varphi_{21,c/s} + \phi_{l,1}$, and $\lambda = \eta_s + \phi_{l,2} - \phi_{12,c}$, with $\eta_{s/c} = [\arg(A_1) \pm \arg(A_2)]/2$ and $\varphi_{nn',c/s} = (\varphi_{r,n} \mp \varphi_{l,n})/2$.

Evidently, the vanishing of the diagonal elements in Eq. (C11), i.e., $\Sigma T_1 = 0$, is the precondition for implementing the single-qubit X or Y gate. Using the concrete form of ΣT_1 in Eq. (C12), this precondition can be reformulated into

$$\cos(g_0 t_{out,1} + \lambda) [\cos \omega_1 \cos \omega_2 - \sin \omega_1 \sin \omega_2] + i \sin(g_0 t_{out,1} + \lambda) [\cos \omega_1 \cos \omega_2 + \sin \omega_1 \sin \omega_2] = 0. \quad (C13)$$

Due to the fact of $\omega_{j=1,2} \in (0, \pi/2]$, it can be inferred that Eq. (C13) holds only under the following two conditions:

$$\sin(g_0 t_{out,1} + \lambda) = 0 \quad (C14)$$

and

$$\cos \omega_1 \cos \omega_2 - \sin \omega_1 \sin \omega_2 = 0 \Rightarrow \Omega = \pi/2, \quad (C15)$$

with $\Omega = \omega_1 + \omega_2$. Under this circumstance, the operation matrix in Eq. (C11) can be further simplified into

$$\mathbf{U}_{2\circlearrowleft} = \begin{pmatrix} 0 & -e^{ig_0 t_{out,2} - iQ_2} \\ e^{-ig_0 t_{out,2} + iQ_2} & 0 \end{pmatrix}. \quad (C16)$$

Then, it follows that $\mathbf{U}_{2\circlearrowleft}$ in Eq. (C16) can be equivalent to the Pauli-X matrix $\mathbf{X} = \begin{pmatrix} 0 & 1 \\ 1 & 0 \end{pmatrix}$ when $|\sin(g_0 t_{out,2} - Q_2)| = 1$. Analogously, the Pauli-Y matrix $\mathbf{Y} = \begin{pmatrix} 0 & -i \\ i & 0 \end{pmatrix}$ can also be realized if $|\sin(g_0 t_{out,2} - Q_2)| = 0$.

Interestingly, when the idling time $t_{out,1}$ meets exclusively the constraint defined in Eq. (C14), $\mathbf{U}_{2\circlearrowleft}$ can be reduced to Eq. (12) of the main text

$$\mathbf{U}_{2\circlearrowleft} = \begin{pmatrix} \cos \Omega e^{ig_0 t_{out,2} + iQ_1} & -\sin \Omega e^{ig_0 t_{out,2} - iQ_2} \\ \sin \Omega e^{-ig_0 t_{out,2} + iQ_2} & \cos \Omega e^{-ig_0 t_{out,2} - iQ_1} \end{pmatrix}. \quad (C17)$$

For $\Omega = (2 \pm 1)\pi/4$, and with $t_{r,2}$ fulfilling $\cos(g_0 t_{out,2} + Q_1) = 0$, it is found that the operation matrix can be mapped to a generalized Hadamard gate

$$\mathbf{H} = \frac{1}{\sqrt{2}} \begin{pmatrix} 1 & e^{i\varphi_0} \\ e^{-i\varphi_0} & -1 \end{pmatrix}. \quad (C18)$$

In contrast to a conventional Hadamard gate, the gate modulation involves an extra phase shift φ_0 given by $\varphi_0 = \tilde{\varphi} \mp \pi/2$, with $\tilde{\varphi} = \pi/2 - Q_1 - Q_2$ and $\Omega = (2 \pm 1)\pi/4$.

* liuzh@baqis.ac.cn
 † liuxf@baqis.ac.cn
 ‡ hqxu@pku.edu.cn

¹ Guido Burkard, Thaddeus D. Ladd, Andrew Pan, John M. Nichol, and Jason R. Petta, Semiconductor spin qubits, Rev. Mod. Phys. **95**, 025003 (2023).

² Anasua Chatterjee, Paul Stevenson, Silvano De Franceschi, Andrea Morello, Nathalie P. de Leon, and Ferdinand Kuemmeth, Semiconductor qubits in practice, *Nat. Rev. Phys.* **3**, 157-177 (2021).

³ Aaron J. Weinstein, Matthew D. Reed, Aaron M. Jones, Reed W. Andrews, David Barnes, Jacob Z. Blumoff, Larken E. Euliss, Kevin Eng, Bryan H. Fong, Sieu D. Ha, Daniel R. Hulbert, Clayton A. C. Jackson, Michael Jura, Tyler E. Keating, Joseph Kerckhoff, Andrey A. Kiselev, Justine Matten, Golam Sabbir, Aaron Smith, Jeffrey Wright, Matthew T. Rakher, Thaddeus D. Ladd, and Matthew G. Borselli, Universal logic with encoded spin qubits in silicon, *Nature* **615**, 817-822 (2023).

⁴ Peter Stano and Daniel Loss, Review of performance metrics of spin qubits in gated semiconducting nanostructures, *Nat. Rev. Phys.* **4**, 672 (2022).

⁵ Akito Noiri, Kenta Takeda, Takashi Nakajima, Takashi Kobayashi, Amir Sammak, Giordano Scappucci, and Seigo Tarucha, Fast universal quantum gate above the fault-tolerance threshold in silicon, *Nature* **601**, 338-342 (2022).

⁶ X. Xue, M. Russ, N. Samkharadze, B. Undseth, A. Sammak, G. Scappucci, and L. M. K. Vandersypen, Quantum logic with spin qubits crossing the surface code threshold, *Nature* **601**, 343-347 (2022).

⁷ P. Steinacker, N. D. Stuyck, W. H. Lim, T. Tanttu, MengKe Feng, S. Serrano, A. Nickl, M. Candido, J. D. Cifuentes, E. Vahapoglu, S. K. Bartee, F. E. Hudson, K. W. Chan, S. Kubicek, J. Jussot, Y. Canvel, S. Beyne, Y. Shimura, R. Loo, C. Godfrin, B. Raes, S. Baudot, D. Wan, A. Laucht, C. H. Yang, A. Saraiva, C. C. Escott, K. De Greve, and A. S. Dzurak, Industry-compatible silicon spin-qubit unit cells exceeding 99% fidelity, *Nature* **646**, 81-87 (2025).

⁸ Adam R. Mills, Charles R. Guinn, Michael J. Gullans, Anthony J. Sigillito, Mayer M. Feldman, Erik Nielsen, Jason R. Petta, Two-qubit silicon quantum processor with operation fidelity exceeding 99%, *Sci. Adv.* **8**, eabn5130 (2022).

⁹ S. G. J. Philips, M. T. Madzik, S. V. Amitonov, S. L. de Snoo, M. Russ, N. Kalhor, C. Volk, W. I. L. Lawrie, D. Brousse, L. Tryputen, B. P. Wuetz, A. Sammak, M. Veldhorst, G. Scappucci, and L. M. K. Vandersypen, Universal control of a six-qubit quantum processor in silicon, *Nature* **609**, 919-924 (2022).

¹⁰ Nico W. Hendrickx, William I. L. Lawrie, Maximilian Russ, Floor van Riggelen, Sander L. de Snoo, Raymond N. Schouten, Amir Sammak, Giordano Scappucci, and Menno Veldhorst, A four-qubit germanium quantum processor, *Nature* **591**, 580-585 (2021).

¹¹ N. W. Hendrickx, D. P. Franke, A. Sammak, G. Scappucci, and M. Veldhorst, Fast two-qubit logic with holes in germanium, *Nature* **577**, 487-491 (2020).

¹² W. I. L. Lawrie, M. Rimbach-Russ, F. van Riggelen, N. W. Hendrickx, S. L. de Snoo, A. Sammak, G. Scappucci, J. Helsen, and M. Veldhorst, Simultaneous single-qubit driving of semiconductor spin qubits at the fault-tolerant threshold, *Nat. Commun.* **14**, 3617 (2023).

¹³ Ada Warren and Sophia E. Economou, Silicon qubits move a step closer to achieving error correction, *Nature* **601**, 320-322 (2022).

¹⁴ R. Xue, M. Beer, I. Seidler, S. Humpohl, J.-S. Tu, S. Trellenkamp, T. Struck, H. Bluhm, and L. R. Schreiber, Si/SiGe QuBus for single electron information-processing devices with memory and micron-scale connectivity function, *Nat. Commun.* **15**, 2296 (2024).

¹⁵ Maxim De Smet, Yuta Matsumoto, Anne-Marije J. Zwerver, Larysa Tryputen, Sander L. de Snoo, Sergey V. Amitonov, Sam R. Katiraei-Far, Amir Sammak, Nodar Samkharadze, Önder Güçlü, Rick N. M. Wasserman, Eliska Greplová, Maximilian Rimbach-Russ, Giordano Scappucci, and Lieven M. K. Vandersypen, High-fidelity single-spin shuttling in silicon, *Nat. Nanotechnol.* **20**, 866-872 (2025).

¹⁶ A. M. J. Zwerver, S.V. Amitonov, S.L. de Snoo, M.T. Madzik, M. Rimbach-Russ, A. Sammak, G. Scappucci, and L.M.K. Vandersypen, Shutting an electron spin through a silicon quantum dot array, *PRX Quantum* **4**, 030303 (2023).

¹⁷ Minjun Jeon, Simon C. Benjamin, and Andrew J. Fisher, Robustness of electron charge shuttling: Architectures, pulses, charge defects, and noise thresholds, *Phys. Rev. B* **111**, 195302 (2025).

¹⁸ V. Langrock, J. A. Krzywda, N. Focke, I. Seidler, L. R. Schreiber, and Ł. Cywiński, Blueprint of a Scalable Spin Qubit Shuttle Device for Coherent Mid-Range Qubit Transfer in Disordered Si/SiGe/SiO₂, *PRX Quantum* **4**, 020305 (2023).

¹⁹ Akito Noiri, Kenta Takeda, Takashi Nakajima, Takashi Kobayashi, Amir Sammak, Giordano Scappucci, and Seigo Tarucha, A shuttling-based two-qubit logic gate for linking distant silicon quantum processors, *Nat. Commun.* **13**, 5740 (2022).

²⁰ D. Fernández, Yue Ban, and G. Platero, Flying Spin Qubits in Quantum Dot Arrays Driven by Spin-Orbit Interaction, *Quantum* **8**, 1533 (2024).

²¹ F. K. Unseld, B. Undseth, E. Raymenants, Y. Matsumoto, S. L. de Snoo, S. Karwal, O. Pietx-Casas, Alexander S. Ivlev, Marcel Meyer, Amir Sammak, Menno Veldhorst, Giordano Scappucci, and Lieven M. K. Vandersypen, Baseband control of single-electron silicon spin qubits in two dimensions, *Nat. Commun.* **16**, 5605 (2025).

²² Chien-An Wang, Valentin John, Hanifa Tidjani, Cécile X. Yu, Alexander S. Ivlev, Corentin Déprez, Floor van Riggelen-Doelman, Benjamin D. Woods, Nico W. Hendrickx, William I. L. Lawrie, Lucas E. A. Stehouwer, Stefan D. Oosterhout, Amir Sammak, Mark Friesen, Giordano Scappucci, Sander L. de Snoo, Maximilian Rimbach-Russ, Francesco Borsoi, Menno Veldhorst, Operating semiconductor quantum processors with hopping spins, *Science* **385**, 447-452 (2024).

²³ V. John, C. X. Yu, B. van Straaten, E. A. R. Mena, M. Rodriguez, S. Oosterhout, L. E. A. Stehouwer, G. Scappucci, S. Bosco, M. R. Russ, Y.-M. Niquet, F. Borsoi, and M. Veldhorst, A two-dimensional 10-qubit array in germanium with robust and localised qubit control, *arXiv:2412.16044*.

²⁴ Matthias Künne, Alexander Willmes, Max Oberländer, Christian Gorjaew, Julian D. Teske, Harsh Bhardwaj, Max Beer, Eugen Kammerloher, René Otten, Inga Seidler, Ran Xue, Lars R. Schreiber, and Hendrik Bluhm, The SpinBus architecture for scaling spin qubits with electron shuttling, *Nat. Commun.* **15**, 4977 (2024).

²⁵ I. Seidler, T. Struck, R. Xue, N. Focke, S. Trellenkamp, H. Bluhm, and L. R. Schreiber, Conveyor-mode single-electron shuttling in Si/SiGe for a scalable quantum computing architecture, *npj Quantum Inf.* **8**, 100 (2022).

²⁶ N. Sato, T. Sekiguchi, T. Utsugi and H. Mizuno, Generating Shutting Procedures for Constrained Silicon Quantum Dot Array, *IEEE Trans. on Quantum Eng.* **6**, 1 (2025).

²⁷ Adam Siegel, Armands Strikis, and Michael Fogarty, A.

Siegel, A. Strikis, and M. Fogarty, Towards Early Fault Tolerance on a $2 \times N$ Array of Qubits Equipped with Shuttling, *PRX Quantum* **5**, 040328 (2024).

²⁸ S. Bosco, Ji Zou, and Daniel Loss, High-Fidelity Spin Qubit Shuttling via Large Spin-Orbit Interactions, *PRX Quantum* **5**, 020353 (2024).

²⁹ O. Crawford, J. R. Cruise, N. Mertig, and M. F. Gonzalez-Zalba, Compilation and scaling strategies for a silicon quantum processor with sparse two-dimensional connectivity, *npj Quantum Inf* **9**, 13 (2023).

³⁰ F. van Riggelen-Doelman, C.-A. Wang, S. L. de Snoo, W. I. L. Lawrie, N. W. Hendrickx, M. Rimbach-Russ, A. Sammak, G. Scappucci, C. Déprez, and Menno Veldhorst, Coherent spin qubit shuttling through germanium quantum dots, *Nat. Commun.* **15**, 5716 (2024).

³¹ X.-F. Liu, Y. Matsumoto, T. Fujita, A. Ludwig, A. D. Wieck, and A. Oiwa, Accelerated Adiabatic Passage of a Single Electron Spin Qubit in Quantum Dots, *Phys. Rev. Lett.* **132**, 027002 (2024).

³² Yadav P. Kandel, Haifeng Qiao, Saeed Fallahi, Geoffrey C. Gardner, Michael J. Manfra, and John M. Nichol, Adiabatic quantum state transfer in a semiconductor quantum-dot spin chain, *Nat. Commun.* **12**, 2156 (2021).

³³ T. Fujita, T. A. Baart, C. Reichl, W. Wegscheider, and L. M. K. Vandersypen, Coherent shuttle of electron-spin states, *npj Quantum Inf.* **3**, 22 (2017).

³⁴ J. R. Petta, H. Lu, and A. C. Gossard, A Coherent Beam Splitter for Electronic Spin States, *Science* **327**, 669 (2010).

³⁵ Gang Cao, Hai-Ou Li, Tao Tu, Li Wang, Cheng Zhou, Ming Xiao, Guang-Can Guo, Hong-Wen Jiang, and Guo-Ping Guo, Ultrafast universal quantum control of a quantum-dot charge qubit using Landau-Zener-Stückelberg interference, *Nat. Commun.* **4**, 1401 (2013).

³⁶ Takeshi Ota, Kenichi Hitachi, and Koji Muraki, Landau-Zener-Stückelberg interference in coherent charge oscillations of a one-electron double quantum dot, *Sci. Rep.* **8**, 5491 (2018).

³⁷ Jakub Łuczak and Bogdan R. Bułka, Landau-Zener transitions in spin qubit encoded in three quantum dots, *Quantum Inf. Process* **16**, 10 (2017).

³⁸ Florian Ginzel, Adam R. Mills, Jason R. Petta, and Guido Burkard, Spin shuttling in a silicon double quantum dot, *Phys. Rev. B* **102**, 195418 (2020).

³⁹ Jonas R. F. Lima and Guido Burkard, Partial Landau-Zener transitions and applications to qubit shuttling, *Phys. Rev. B* **111**, 235439 (2025).

⁴⁰ Yi-Chao Li, Xi Chen, J. G. Muga, and E. Ya Sherman, Qubit gates with simultaneous transport in double quantum dots, *New J. Phys.* **20**, 11302 (2018).

⁴¹ Yi-Chao Li, D. Martínez-Cercós, S. Martínez-Garaot, Xi Chen, and J. G. Muga, Hamiltonian design to prepare arbitrary states of four-level systems, *Phys. Rev. A* **97**, 013830 (2018).

⁴² Jingwei Mu, Shaoyun Huang, Ji-Yin Wang, Guang-Yao Huang, Xuming Wang and H. Q. Xu, Measurements of anisotropic g-factors for electrons in InSb nanowire quantum dots, *Nanotechnology* **32**, 020002 (2021).

⁴³ Ting Zhang, He Liu, Fei Gao, Gang Xu, Ke Wang, Xin Zhang, Gang Cao, Ting Wang, Jianjun Zhang, Xuedong Hu, Hai-Ou Li, and Guo-Ping Guo, Anisotropic g-Factor and Spin-Orbit Field in a Germanium Hut Wire Double Quantum Dot, *Nano Lett.* **21**, 3835-3842 (2021).

⁴⁴ N. W. Hendrickx, L. Massai, M. Mergenthaler, F. J. Schupp, S. Paredes, S. W. Bedell, G. Salis, and A. Fuhrer, Sweet-spot operation of a germanium hole spin qubit with highly anisotropic noise sensitivity, *Nat. Mater.* **23**, 920-927 (2024).

⁴⁵ J. van Bree, A. Yu. Silov, M. L. van Maasakkers, C. E. Pryor, M. E. Flatté, and P. M. Koenraad, Anisotropy of electron and hole g tensors of quantum dots: An intuitive picture based on spin-correlated orbital currents, *Phys. Rev. B* **93**, 035311 (2016).

⁴⁶ Y. Serov, A. Galimov, D. S. Smirnov, G. Klimko, S. Sorokin, Y. Zadiranov, I. Sedova, M. Rakhlis, D. Berezhina, N. Leppenen, Y. Salii, M. Kulagina, S. Troshkov, T. V. Shubina, and A. A. Toropov, Hidden anisotropy controls spin-photon entanglement in a charged quantum dot, *Phys. Rev. Applied* **23**, 044019 (2025).

⁴⁷ G.E. Pikus and F.G. Pikus, The mechanism of heavy and light hole mixing in GaAs/AlAs superlattices, *Solid State Commun.* **89**, 319 (1994).

⁴⁸ A. V. Trifonov, I. A. Akimov, C. Sgroi, L. E. Golub, A. Ludwig, E. L. Ivchenko, I. A. Yugova, A. D. Wieck, D. R. Yakovlev, A. N. Kosarev, S. E. Scholz, and M. Bayer, Homogeneous optical anisotropy in an ensemble of In-GaAs quantum dots induced by strong enhancement of the heavy-hole band Landé parameter, *Phys. Rev. B* **104**, L161405 (2021).

⁴⁹ Oleg N. Jouravlev and Yuli V. Nazarov, Electron Transport in a Double Quantum Dot Governed by a Nuclear Magnetic Field, *Phys. Rev. Lett.* **96**, 176804 (2006).

⁵⁰ W. A. Coish and Daniel Loss, Singlet-triplet decoherence due to nuclear spins in a double quantum dot, *Phys. Rev. B* **72**, 125337 (2005).

⁵¹ M. J. A. Schuetz, E. M. Kessler, L. M. K. Vandersypen, J. I. Cirac, and G. Giedke, Nuclear spin dynamics in double quantum dots: Multistability, dynamical polarization, criticality, and entanglement, *Phys. Rev. B* **89**, 195310 (2014).

⁵² M. M. Glazov, Spin noise of localized electrons: Interplay of hopping and hyperfine interaction, *Phys. Rev. B* **91**, 195301 (2015).

⁵³ A. V. Shumilin and V. V. Kabanov, Kinetic equations for hopping transport and spin relaxation in a random magnetic field, *Phys. Rev. B* **92**, 014206 (2015).

⁵⁴ V. N. Mantsevich and D. S. Smirnov, Universal power law decay of spin polarization in double quantum dot, *Phys. Rev. B* **100**, 075409 (2019).

⁵⁵ Jo-Tzu Hung, Łukasz Cywinski, Xuedong Hu, and S. Das Sarma, Hyperfine interaction induced dephasing of coupled spin qubits in semiconductor double quantum dots, *Phys. Rev. B* **88**, 085314 (2013).

⁵⁶ Jan Fischer and Daniel Loss, Hybridization and Spin Decoherence in Heavy-Hole Quantum Dots, *Phys. Rev. Lett.* **105**, 266603 (2010).

⁵⁷ C. Testelin, F. Bernardot, B. Eble, and M. Chamarro, Hole-spin dephasing time associated with hyperfine interaction in quantum dots, *Phys. Rev. B* **77**, 195440 (2009).

⁵⁸ S. M. Huang, Y. Tokura, H. Akimoto, K. Kono, J. J. Lin, S. Tarucha, and K. Ono, Spin Bottleneck in Resonant Tunneling through Double Quantum Dots with Different Zeeman Splittings, *Phys. Rev. Lett.* **104**, 136801 (2010).

⁵⁹ Simon Geyer, Bence Hetényi, Stefano Bosco, Leon C. Camenzind, Rafael S. Eggl, Andreas Fuhrer, Daniel Loss, Richard J. Warburton, Dominik M. Zumbühl, and Andreas V. Kuhlmann, Anisotropic exchange interaction of two hole-spin qubits, *Nature Physics* **20**, 1152-1157 (2024).

⁶⁰ J. Danon and Yu. V. Nazarov, Pauli spin blockade in the

presence of strong spin-orbit coupling, *Phys. Rev. B* **80**, 041301(R) (2009).

⁶¹ Stefano Bosco, Bence Hetenyi, and Daniel Loss, Hole Spin Qubits in Si FinFETs With Fully Tunable Spin-Orbit Coupling and Sweet Spots for Charge Noise, *PRX Quantum* **2**, 010348 (2021).

⁶² Rui Li and J. Q. You, Anisotropic exchange coupling in a nanowire double quantum dot with strong spin-orbit coupling, *Phys. Rev. B* **90**, 035303 (2014).

⁶³ Zhi-Hai Liu, O. Entin-Wohlman, A. Aharony, and J. Q. You, Control of the two-electron exchange interaction in a nanowire double quantum dot, *Phys. Rev. B* **98**, 241303(R) (2018).

⁶⁴ R. I. Shekhter, O. Entin-Wohlman, M. Jonson, and A. Aharony, Magnetoconductance Anisotropies and Aharonov-Casher Phases, *Phys. Rev. Lett.* **129**, 037704 (2022).

⁶⁵ O. Entin-Wohlman and A. Aharony, Spin geometric phases in hopping magnetoconductance, *Phys. Rev. Research* **1**, 033112 (2019).

⁶⁶ Zhi-Hai Liu, O. Entin-Wohlman, A. Aharony, J. Q. You, and H. Q. Xu, Topological states and interplay between spin-orbit and Zeeman interactions in a spinful Su-Schrieffer-Heeger nanowire, *Phys. Rev. B* **104**, 085302 (2021).

⁶⁷ L. DiCarlo, H. J. Lynch, A. C. Johnson, L. I. Childress, K. Crockett, and C. M. Marcus M. P. Hanson and A. C. Gossard, Differential Charge Sensing and Charge Delocalization in a Tunable Double Quantum Dot, *Phys. Rev. Lett.* **92**, 226801 (2004).

⁶⁸ Xinyu Zhao and Xuedong Hu, Measurement of Tunnel Coupling in a Si Double Quantum dot Based on Charge Sensing, *Phys. Rev. Applied* **17**, 064043 (2022).

⁶⁹ Yi Luo, Xiao-Fei Liu, Zhi-Hai Liu, Weijie Li, Shili Yan, Han Gao, Haitian Su, Dong Pan, Jianhua Zhao, Ji-Yin Wang, and Hongqi Xu, One-dimensional quantum dot array integrated with charge sensors in an InAs nanowire, *Nano Lett.* **24**, 44, 14012-14019 (2024).

⁷⁰ S.N. Shevchenko, S. Ashhab, and Franco Nori, Landau-Zener-Stückelberg interferometry, *Physics Reports* **492**, 1 (2010).

⁷¹ C. Wittig, The Landau-Zener formula, *J. Phys. Chem. B* **109**, 8428 (2005).

⁷² J. A. Krzywda and Lukasz Cywinski, Decoherence of electron spin qubit during transfer between two semiconductor quantum dots at low magnetic fields, *Phys. Rev. B* **111**, 115305 (2025).

⁷³ Guozhu Sun, Xueda Wen, Ming Gong, Dan-Wei Zhang, Yang Yu, Shi-Liang Zhu, Jian Chen, Peiheng Wu, and Siyuan Han, Observation of coherent oscillation in single-passage Landau-Zener transitions, *Sci. Rep.* **5**, 8463 (2015).

⁷⁴ Lian-Ao Wu and Daniel A. Lidar, Universal quantum logic from Zeeman and anisotropic exchange interactions, *Phys. Rev. A* **66**, 062314 (2002).

⁷⁵ Maximilian Russ, D. M. Zajac, A. J. Sigillito, F. Borjans, J. M. Taylor, J. R. Petta, and Guido Burkard, High-fidelity quantum gates in Si/SiGe double quantum dots, *Phys. Rev. B* **97**, 085421 (2018).

⁷⁶ M. Veldhorst, C. H. Yang, J. C. C. Hwang, W. Huang, J. P. Dehollain, J. T. Muhonen, S. Simmons, A. Laucht, F. E. Hudson, K. M. Itoh, A. Morello, and A. S. Dzurak, A two-qubit logic gate in silicon, *Nature* **526**, 410-414 (2015).

⁷⁷ Jiaan Qi, Zhi-Hai Liu and Hongqi Xu, Spin-orbit interaction enabled high-fidelity two-qubit gates, *New J. Phys.* **26**, 013012 (2024).

⁷⁸ Zhanning Wang, Elizabeth Marcellina, Alex. R. Hamilton, James H. Cullen, Sven Rogge, Joe Salfi, and Dimitrie Culcer, Optimal operation points for ultrafast, highly coherent Ge hole spin-orbit qubits, *npj Quantum Information* **7**, 54 (2021).

⁷⁹ Abhikbrata Sarkar, Zhanning Wang, Matthew Rendell, Nico W. Hendrickx, Menno Veldhorst, Giordano Scappucci, Mohammad Khalifa, Joe Salfi, Andre Saraiva, A. S. Dzurak, A. R. Hamilton, and Dimitrie Culcer, *Phys. Rev. B* **108**, 245301 (2023).

⁸⁰ Vitaly N. Golovach, Alexander Khaetskii, and Daniel Loss, Phonon-Induced Decay of the Electron Spin in Quantum Dots, *Phys. Rev. Lett.* **93**, 016601 (2004).

⁸¹ Franziska Maier, Christoph Kloeffel, and Daniel Loss, Tunable *g* factor and phonon-mediated hole spin relaxation in Ge/Si nanowire quantum dots, *Phys. Rev. B* **87**, 161305(R) (2013).

⁸² Zhi-Hai Liu, Rui Li, Xuedong Hu, and J. Q. You, Spin-orbit coupling and electric-dipole spin resonance in a nanowire double quantum dot, *Sci. Rep.* **8**, 2302 (2018).

⁸³ Hanifa Tidjani, Alberto Tosato, Alexander Ivlev, Corentin Déprez, Stefan Oosterhout, Lucas Stehouwer, Amir Sammak, Giordano Scappucci, and Menno Veldhorst, Vertical gate-defined double quantum dot in a strained germanium double quantum well, *Phys. Rev. Applied* **20**, 054035 (2023).

⁸⁴ R. Winkler, *Spin-orbit Coupling Effects in Two-dimensional Electron and Hole Systems* (Springer, Berlin, 2003).

⁸⁵ Chun-Xiao Liu, Guanzhong Wang, Tom Dvir, and Michael Wimmer, Tunable Superconducting Coupling of Quantum Dots via Andreev Bound States in Semiconductor-Superconductor Nanowires, *Phys. Rev. Lett.* **129**, 267701 (2022).